



ARL-TR-7953 • FEB 2017



Considerations for Explosively Driven Conical Shock Tube Design: Computations and Experiments

by Joel B Stewart

Approved for public release; distribution is unlimited.

NOTICES

Disclaimers

The findings in this report are not to be construed as an official Department of the Army position unless so designated by other authorized documents.

Citation of manufacturer's or trade names does not constitute an official endorsement or approval of the use thereof.

Destroy this report when it is no longer needed. Do not return it to the originator.



Considerations for Explosively Driven Conical Shock Tube Designs: Computations and Experiments

by Joel B Stewart

Weapons and Materials Research Directorate, ARL

REPORT DOCUMENTATION PAGE				Form Approved OMB No. 0704-0188	
<p>Public reporting burden for this collection of information is estimated to average 1 hour per response, including the time for reviewing instructions, searching existing data sources, gathering and maintaining the data needed, and completing and reviewing the collection information. Send comments regarding this burden estimate or any other aspect of this collection of information, including suggestions for reducing the burden, to Department of Defense, Washington Headquarters Services, Directorate for Information Operations and Reports (0704-0188), 1215 Jefferson Davis Highway, Suite 1204, Arlington, VA 22202-4302. Respondents should be aware that notwithstanding any other provision of law, no person shall be subject to any penalty for failing to comply with a collection of information if it does not display a currently valid OMB control number.</p> <p>PLEASE DO NOT RETURN YOUR FORM TO THE ABOVE ADDRESS.</p>					
1. REPORT DATE (DD-MM-YYYY) February 2017		2. REPORT TYPE Technical Report		3. DATES COVERED (From - To) September 2015–November 2016	
4. TITLE AND SUBTITLE Considerations for Explosively Driven Conical Shock Tube Design: Computations and Experiments				5a. CONTRACT NUMBER	
				5b. GRANT NUMBER	
				5c. PROGRAM ELEMENT NUMBER	
6. AUTHOR(S) Joel B Stewart				5d. PROJECT NUMBER	
				5e. TASK NUMBER	
				5f. WORK UNIT NUMBER	
7. PERFORMING ORGANIZATION NAME(S) AND ADDRESS(ES) US Army Research Laboratory ATTN: RDRL-WMP-G Aberdeen Proving Ground, MD 21005-5069				8. PERFORMING ORGANIZATION REPORT NUMBER ARL-TR-7953	
9. SPONSORING/MONITORING AGENCY NAME(S) AND ADDRESS(ES)				10. SPONSOR/MONITOR'S ACRONYM(S)	
				11. SPONSOR/MONITOR'S REPORT NUMBER(S)	
12. DISTRIBUTION/AVAILABILITY STATEMENT Approved for public release; distribution is unlimited.					
13. SUPPLEMENTARY NOTES					
14. ABSTRACT <p>This report covers computational and experimental work related to the development and design of explosively driven conical shock tubes. The first part of the report focuses on using Lawrence Livermore National Laboratory's ALE3D shock physics code to replicate previous experimental results obtained from a 17° (full angle) shock tube. Next, a computational parameter study of various shock tube design choices, such as shock tube angle and explosive charge geometry, on the resulting air blast is detailed. Finally, experimental data using a new 10° shock tube along with some of the driver section design choices investigated in the computational parameter study is presented.</p>					
15. SUBJECT TERMS shock tube, air blast, hydrocode, explosively driven shock tube, explosive					
16. SECURITY CLASSIFICATION OF:			17. LIMITATION OF ABSTRACT UU	18. NUMBER OF PAGES 52	19a. NAME OF RESPONSIBLE PERSON Joel B Stewart
a. REPORT Unclassified	b. ABSTRACT Unclassified	c. THIS PAGE Unclassified			19b. TELEPHONE NUMBER (Include area code) 410-278-3129

Contents

List of Figures	iv
List of Tables	vii
Acknowledgments	viii
1. Introduction	1
2. Computations vs Previous Experiments: 17° Conical Shock Tube	3
3. Shock Tube Parametric Computational Study	7
3.1 On the Influence of Driver Section and Charge Design: 10° Conical Shock Tube	8
3.2 On the Influence of Cone Angle	18
4. 10° Shock Tube: Computational and Experimental Results	20
4.1 Computational Predictions vs Experimental Results	22
4.2 Mitigation of Release Waves at the Exit Section	28
5. Conclusions	34
6. References	35
Appendix. 10° Shock Tube Pencil Gauge Data	36
List of Symbols, Abbreviations, and Acronyms	40
Distribution List	41

List of Figures

Fig. 1	Zoomed-in view of the ALE3D shock tube entry section geometry (the red material represents C4 and the gray represents the steel shock tube), which was used to replicate experimental data presented in Stewart and Pecora (2015).....	4
Fig. 2	Comparison of computational vs experimental data on the axis of symmetry and at the exit (192 cm from the nearest surface of the C4 explosive driver charge) of a 17° shock tube (a) overpressure and (b) impulse per unit area.....	5
Fig. 3	Comparison of experimental vs computational data 15 cm off the axis of symmetry and at the exit (192 cm from the nearest surface of the C4 explosive driver charge) of a 17° shock tube (a) overpressure and (b) impulse per unit area.....	6
Fig. 4	Schematic of shock tube driver section for reference with Table 1.....	10
Fig. 5	Zoomed-in view of the ALE3D shock tube entry section geometry for the baseline shock tube design (the red material represents pentolite, the gray represents the steel shock tube, and the blue represents the air).....	10
Fig. 6	Pressure loading measured 2.0 m downstream of the driver charge surface for the baseline design of the 10° shock tube driver section and 5-g driver charge compared with a Friedlander waveform obtained from CONWEP for a 544-g (1.2-lb) pentolite charge.....	11
Fig. 7	Influence of driver charge mass on the pressure profile of the 10° shock tube measured 2.0 m downstream of the driver charge surface (a) fixed aspect ratio ($L/D = 1$) and (b) fixed charge diameter ($D = 16.0$ mm).....	13
Fig. 8	Influence of a backing plate behind the 5-g driver charge on the pressure profile of the 10° shock tube measured 2.0 m downstream of the driver charge surface.....	14
Fig. 9	Influence of various modifications to the driver section and 5-g driver charge on the pressure profile of the 10° shock tube measured 2.0 m downstream of the driver charge surface.....	15
Fig. 10	Pressure contours at 2 μ s after detonation showing the detonation wave and shock reflections through the explosive driver charge (red boundary line) for the baseline case with no air gap between the driver charge and the steel walls (bottom half) and for the case with a 2-mm air gap (top half).....	16
Fig. 11	Influence of shock tube cone angle on the pressure profile measured 2.0 m downstream of the driver charge surface.....	19
Fig. 12	Comparison of pressure contours at the approximate times when the primary blast wave has traveled 2.0 m inside the shock tube: (a) 10° cone (2.1 ms) and (b) 30° cone (1.5 ms).....	20

Fig. 13	Shock tube basic engineering drawings (dimensions are in inches): (a) driver housing section, (b) 10° conical driver transition section, and (c) 10° conical body section including the cylindrical exit section	22
Fig. 14	10° shock tube, without the cylindrical exit section	23
Fig. 15	Example shock tube driver section used in an experiment: (a) (from left to right) pentolite explosive charge, blue foam centering device, cylindrical driver housing section, and conical driver transition section prior to the experiment; (b) driver housing section and driver transition section postexperiment	24
Fig. 16	Comparison of experimental vs computational data on the axis of symmetry and at the exit (2.16 m from the nearest surface of the pentolite explosive driver charge) of a 10° shock tube: (a) overpressure and (b) impulse per unit area.....	26
Fig. 17	Comparison of experimental vs computational data 10 cm off the axis of symmetry and at the exit (2.16 m from the nearest surface of the pentolite explosive driver charge) of a 10° shock tube: (a) overpressure and (b) impulse per unit area.....	27
Fig. 18	10° shock tube, with the cylindrical exit section attached	29
Fig. 19	Comparison of experimental data on the axis of symmetry and at the exit (2.16 m from the nearest surface of the 5-g pentolite explosive driver charge) of a 10° shock tube with an exit section vs a Friedlander waveform: (a) overpressure and (b) impulse per unit area	30
Fig. 20	Comparison of experimental data 10 cm off the axis of symmetry and at the exit (2.16 m from the nearest surface of the 5-g pentolite explosive driver charge) of a 10° shock tube with an exit section vs a Friedlander waveform: (a) overpressure and (b) impulse per unit area	31
Fig. 21	Shock tube experimental air blast data due to a 5-g pentolite charge at various locations compared with the Friedlander waveforms at corresponding locations for an 1814-g pentolite charge: (a) without an exit section and (b) with an exit section.....	33
Fig. A-1	Experimental data from pencil gauges inserted 6 inches inside the shock tube's conical exit (i.e., 2.00 m from the charge surface), with no cylindrical exit section. Data are shown from 2 experiments, both on and 102-mm off-axis.....	37
Fig. A-2	Experimental data from pencil gauges inserted at the shock tube's conical exit (i.e., 2.16 m from the charge surface), with no cylindrical exit section. Data are shown from 2 experiments, both on and 102-mm off-axis.....	37

Fig. A-3	Experimental data from pencil gauges inserted 6 inches outside the conical shock tube's exit (i.e., 2.31 m from the charge surface), with no cylindrical exit section. Data are shown from 2 experiments, both on and 102-mm off-axis.....	38
Fig. A-4	Experimental data from pencil gauges inserted at the shock tube's conical exit (i.e., 2.16 m from the charge surface), when a cylindrical exit section is used. Data are shown from 2 experiments, both on and 102-mm off-axis.....	38
Fig. A-5	Experimental data from pencil gauges inserted 6 inches outside the conical shock tube's exit (i.e., 2.31 m from the charge surface), when a cylindrical exit section is used. Data are shown from 2 experiments, both on and 102 mm off-axis.....	39

List of Tables

Table 1	Computational test matrix for 10° shock tube study.....	9
Table 2	Peak pressures (gauge) in 10° shock tube study	17
Table 3	Computational test matrix for shock tube cone angle study	18

Acknowledgments

I would like to acknowledge Ms Rachel Ehlers for initiating this research into explosively driven shock tubes and facilitating the various programs covered under this report. Drs Scott Kukuck and Barrie Homan made themselves available for technical discussions during all phases of this work, and I appreciate their insight and feedback. Mr Stephen Schraml provided a technical review for this report, and his feedback greatly improved its quality. For the experiments involving the 10° shock tube, I would like to acknowledge Mr Paul Duvall and Mr Benjamin Showalter as the test directors; Mr James Racine, Mr Rick Rapposelli, Mr Larry Stevenson, and Mr Charles Wilhelm for range setup and execution; Dr Brian Roos and Ms Dawnn Megonnell for coordination and fabrication of explosive charges; Mr James Gyolai and Mr Bobby Hall at the US Army Research Laboratory (ARL) machine shop for fabricating the shock tube driver sections; Mr Robert Bruce for coordination and Mr David Weyand for press-braking the shock tube body section and fabricating the steel part of the shock tube stand at the ARL weld shop; and Mr Gerard Chaney at the ARL wood shop for fabricating the foam centering devices and the wooden stand.

1. Introduction

Shock tubes have been used for more than a century to provide a controlled, repeatable environment to investigate shock waves travelling through various media and the interaction of these shock waves with other structures (Henshall 1957). Shock tubes generally fall into one of the following categories: 1) gas-driven shock tubes, where high-pressure gases combined with a burst disc result in a shock wave; or 2) explosively driven shock tubes, where an explosive charge generates the shock wave. The challenges associated with operating the different types of shock tubes and accurately producing the particular waveforms of interest have been listed elsewhere (e.g., Courtney et al. 2012), but a limited list of advantages and disadvantages for explosively driven shock tubes specifically is as follows:

Advantages:

- Expensive diagnostic equipment can be shielded from violent detonative events.
- Researchers can study near-field (i.e., prior to shock separation from explosive product gases into air) as well as mid-field (the region where product gases, in addition to the air shock, contribute to the loading) and far-field (the region where only the air shock contributes to the loading) effects.
- Researchers can investigate nonideal explosive effects (e.g., late-time burning).

Disadvantages:

- Explosive handling is a safety risk requiring specialized facilities and personnel.
- The explosively driven flow field must transition through the near and mid-fields, even for projects that are only interested in far-field effects.

Stewart and Pecora (2015) investigated the use of a conical shock tube (1.933 m long with a 17° full cone angle) with an explosive driver charge to approximate the free-field shock moving through air (commonly referred to as air blast) due to a large (relative to the explosive driver charge) explosive detonation. The work documented in this report seeks to build upon the previous work by looking in more detail at various modifications to the explosive driver charge, the driver section (i.e., the portion of the tube that confines the explosive charge and transitions to the body section), and the shock tube's body section (i.e., the portion of the shock tube

designed to confine the air blast). Specifically, the influence of these modifications on the air blast downstream of the shock tube's driver section will be investigated. All pressures listed in this report are overpressures, and all reported impulses are obtained by integrating these overpressures over time (i.e., impulse per unit area).

Pressure time histories due to air blast have a distinct shape. Friedlander (1946) suggested an equation to describe the shock profile that agrees well with experimental data after the air blast separates from the explosive product gases. When dealing with large peak overpressures (above 1 atm), Dewey (2010) recommends the following modified form of the Friedlander waveform:

$$P(t) = P_s e^{-\alpha \left(1 - \frac{t}{t^+}\right)}, \quad (1)$$

where P is the time-dependent overpressure at the gauge location, P_s is the peak overpressure, t is the time after the air blast arrival, t^+ is the positive phase duration, and α is a fitting parameter (the original Friedlander equation may be recovered by setting $\alpha = 1/t^+$).

The Friedlander waveform is an idealized representation of a free-field air blast, without any influence of shock reflections (either from the ground or from shock tube surfaces). Since the shock tube is a tool designed to approximate the free-field air blast, it is instructive to compare the shock tube data back to a Friedlander waveform. Therefore, in some of the plots contained in this report, shock tube experimental and computational data are compared against the modified Friedlander waveform of Eq. 1. For the comparison, P_s and distance from the charge to the gauge location are obtained from the experiment or computation while the corresponding values of t^+ and α are obtained from ConWep (Hyde 1988). The air blast time of arrival, t_0 , is adjusted to line up with the data being compared against (typically, t_0 needs to be adjusted on the order of 10% to line up with the shock tube data).

The Lawrence Livermore National Laboratory shock physics code ALE3D (Nichols 2014) was used for all computations shown in this report. All computations were performed in 2-D axisymmetry with 0.5 mm per square computational zone. This mesh resolution resulted in problem sizes ranging from approximately 10 to 30 million elements, with the shock tube problem requiring increasingly larger computational domains as the shock tube angle is increased. The arbitrary Lagrangian-Eulerian (ALE) formulation was used in all calculations to weight the mesh toward the steel shock tube walls as well as toward the shock front by assigning a higher weight to the artificial viscosity in the air.

When dealing with finite element codes, it is good practice to conduct a mesh resolution study to ensure that the metric of interest (e.g., peak pressure at a certain location) has adequately converged for the mesh resolution being employed (i.e., the solution should be mesh independent). Unfortunately, such a study was not feasible for this work. The combination of thin shock tube walls (on the order of millimeters), small charge size (on the order of centimeters), long shock tube length (on the order of meters), and prolonged event duration (on the order of milliseconds) makes this problem challenging from a computational standpoint. Because of these challenges and the absence of a mesh resolution study, no claim is being made that the solutions presented in this report are fully resolved; the peak pressures and impulses would almost certainly increase if higher-density computational meshes could be afforded. However, the computational goal of this work was to use ALE3D as an iterative design tool for obtaining qualitative trends and yielding more informed design decisions. Roughly speaking, this goal translated into the general rule of being able to run a single computation with a specific shock tube design within 24 h on 1000 processors.

This report is organized as follows: Section 2 focuses on computationally reproducing experimental results from Stewart and Pecora's 17° shock tube. Next, Section 3.1 details a computational study investigating various modifications to the explosive driver charge and inert driver section for a 10° conical shock tube. Section 3.2 continues the parametric study by considering the influence of cone angle on the downstream air blast profile. Finally, experimental results for a 10° conical shock tube with a specific driver charge and driver section geometry are presented in Section 4 and compared against computational results; Section 4.2 investigates preliminary work on alleviating release waves at the shock tube exit section (where test items would typically be placed).

2. Computations vs Previous Experiments: 17° Conical Shock Tube

Prior to conducting a computational study on geometries for which no experimental data exist, an attempt was made to ensure that the experimental data presented in Stewart and Pecora (2015) could be replicated computationally with reasonable accuracy. The shock tube in that article used a 14.5-g cylindrical Composition C4 (C4) driver charge, 28.2 mm in diameter and 15.2 mm long, placed with its rear surface flush with the entry of a 17° conical steel driver section. All cone angles listed in this report refer to the full angle of the conical section. The minimum diameter at the entry of the driver section was 32.0 mm, with a 101.6-mm outer diameter, and both ends of the shock tube were open to the air. Figure 1 shows a schematic of the geometry used to perform the computations; these computations

neglected both the blue foam centering device for the explosive charge and the Teledyne RISI RP-83 detonator. The driver section shown in Fig. 1 consists of a steel cylinder with a conical interior, which houses the C4 driver charge (red) and transitions after 233.2 mm to the constant 4.8-mm-thick steel body section. For computational purposes, a Jones-Wilkes-Lee (JWL) model was used to describe the C4 product gases (an initial density of 1.52 g/cm^3 was assumed, consistent with the experimental estimate), and detonation was described using programmed burn with point initiation at the center of the back surface. Air was described using a tabular equation of state (EOS), and the steel was modeled as 4340 steel using a Steinberg-Guinan rate-independent strength model with a Mie-Grüneisen EOS.

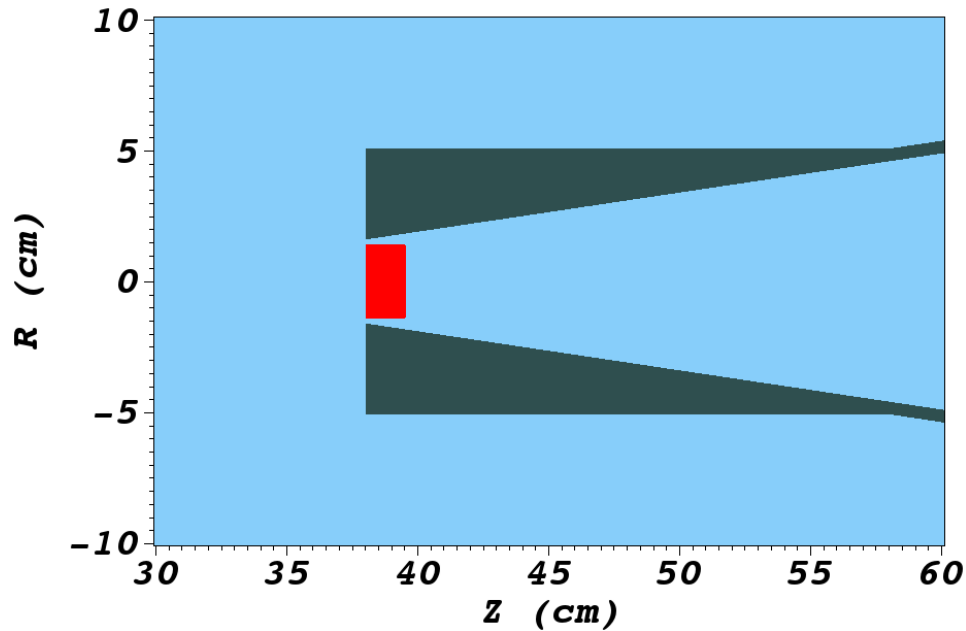
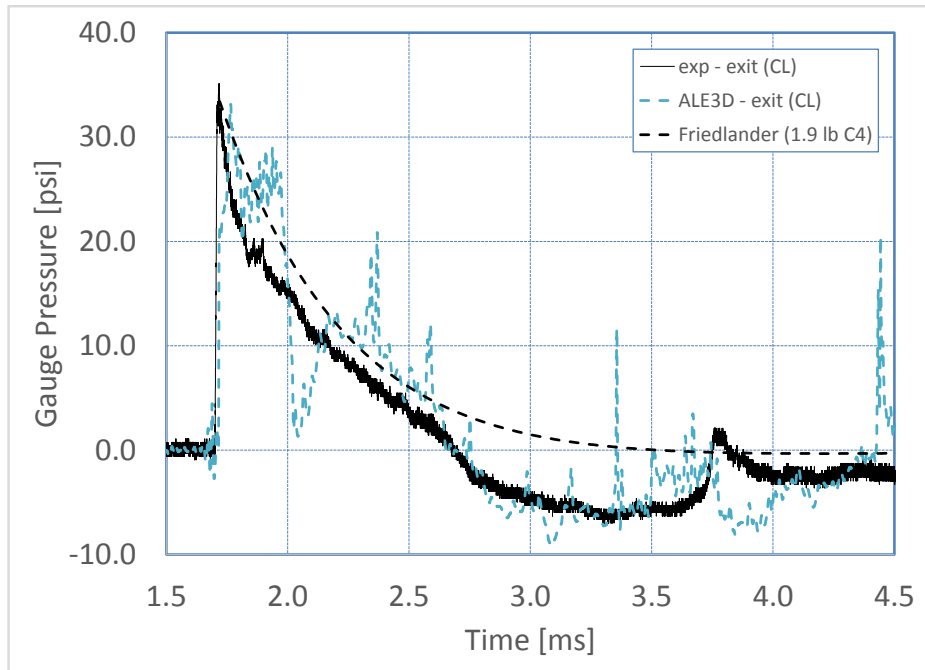
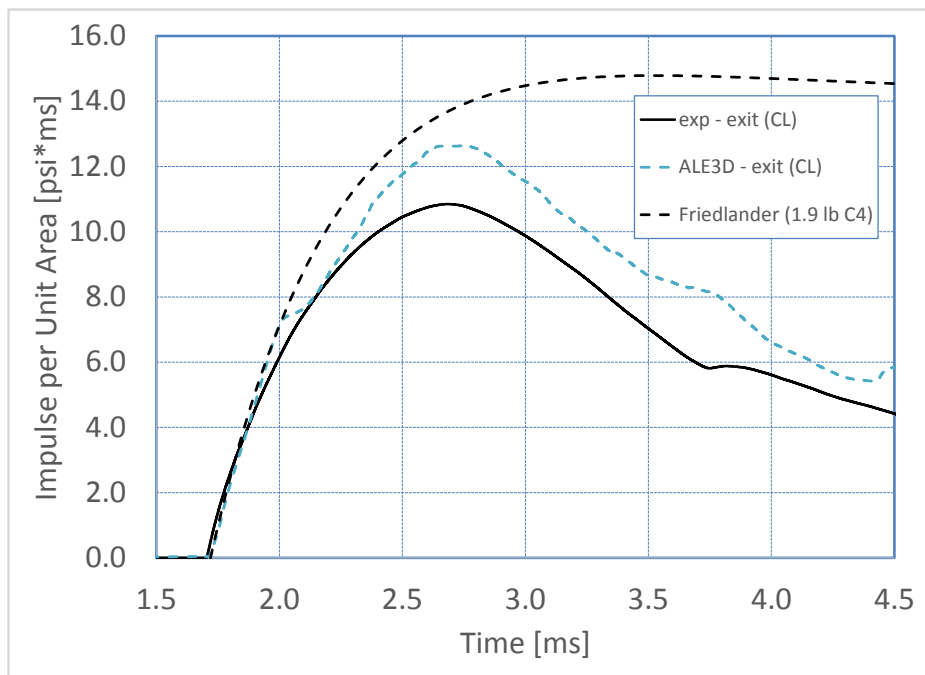


Fig. 1 Zoomed-in view of the ALE3D shock tube entry section geometry (the red material represents C4 and the gray represents the steel shock tube), which was used to replicate experimental data presented in Stewart and Pecora (2015)

A comparison of the computational results with experimental results, taken from shot 7 of Stewart and Pecora (2015), is shown in Figs. 2 and 3 along with a modified Friedlander waveform taken from ConWep and corresponding to the free-field detonation of an 861.8-g (1.9-lb) sphere of C4 at the specified gauge distance from the charge. The shock tube loading profiles undershoot the Friedlander waveform once release waves from the shock tube exit arrive at the gauge locations. All data are taken at the exit of the 1.933-m-long shock tube (i.e., 1.918 m from the closest surface of the C4 charge), where the inner diameter of the shock tube is 0.61 m. Figure 2 shows results on the axis (also referred to as the centerline, or “CL” in the plots), and Fig. 3 shows results 0.15 m off-axis (referred to as “OA” in the plots).

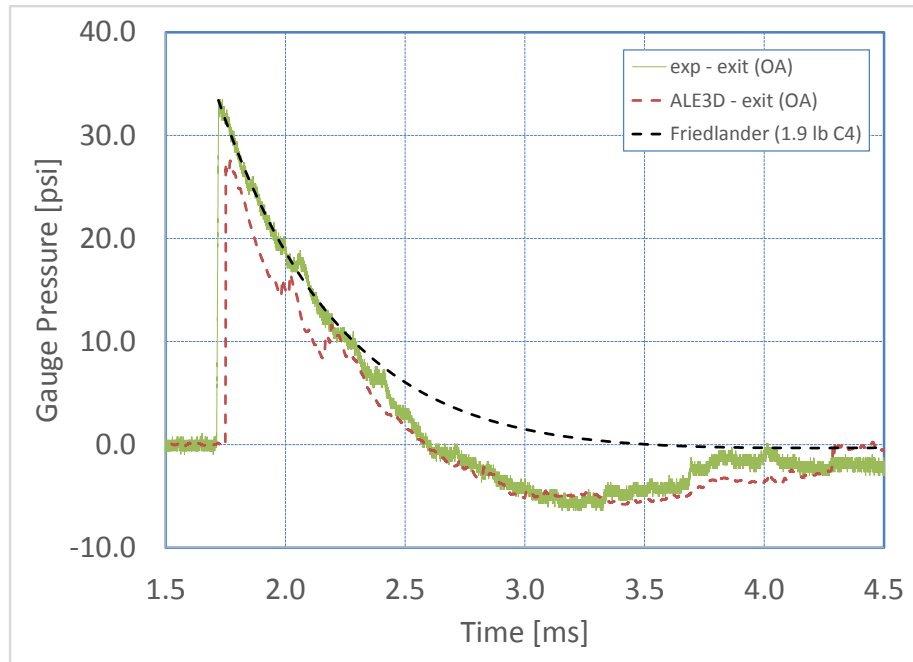


(a)

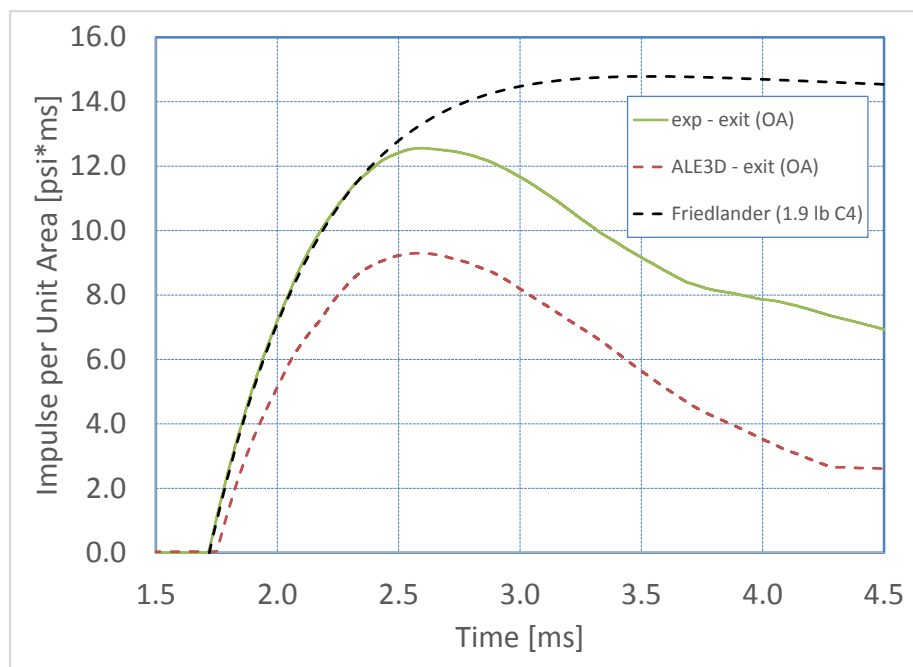


(b)

Fig. 2 Comparison of computational vs experimental data on the axis of symmetry and at the exit (192 cm from the nearest surface of the C4 explosive driver charge) of a 17° shock tube (a) overpressure and (b) impulse per unit area



(a)



(b)

Fig. 3 Comparison of experimental vs computational data 15 cm off the axis of symmetry and at the exit (192 cm from the nearest surface of the C4 explosive driver charge) of a 17° shock tube (a) overpressure and (b) impulse per unit area

The ALE3D computational results shown in Figs. 2 and 3 do a reasonable job of replicating the experimental data in terms of the peak pressure, time of arrival, and impulse (per unit area). The arrival of release waves from the shock tube exit, resulting in a pronounced negative pressure phase, is captured in the ALE3D calculation (the Friedlander waveform does not exhibit this behavior since release waves due to exiting the shock tube would not be present in a free-field detonation). The computational pressure profile on the axis yields a complex shock structure not seen in either the on-axis experimental results or the off-axis results (see Figs. 2a and 3a). This noisy on-axis computational result is consistent with experience, increases with mesh refinement, and is believed to arise from numerical difficulties due to the axisymmetric treatment (e.g., elements along the axis contain very little mass/volume, especially as the mesh is refined, and the mass inside a single element increases substantially as one progresses radially away from the axis). The on-axis computational impulse overshoots the experimental result while the off-axis impulse undershoots the experiment (see Figs. 2b and 3b). In general, the ALE3D computational results were deemed to qualitatively replicate the experimental data sufficiently well to warrant proceeding with the parametric study.

3. Shock Tube Parametric Computational Study

The ALE3D computational approach discussed in the previous sections was shown to replicate the main features of the experimental data when using a 17° conical shock tube along with a C4 driver charge. This same computational approach is used in the current section to investigate the influence that various shock tube design choices have on the resultant loading profile downstream of the explosive charge. All explosive charges used in the work presented in this and all subsequent sections are 50/50 pentolite (modeled using a JWL EOS with programmed burn) as opposed to the C4 used in Section 2. This change was made because of experimental considerations related to the work presented in Section 4 (pentolite is castable and should lead to increased repeatability compared to the putty-like C4). The explosive charge, as in the previous section, has the detonation initiated at a point located at the center of the back surface. The initial density of the pentolite is taken to be 1.56 g/cm³ for the computational study presented in this section. For the rest of this report, the driver section of the shock tube is often referred to as 2 separate sections: 1) the piece housing the explosive charge, which is denoted as the driver housing section, and 2) the part connecting the driver housing section with the body section of the shock tube, which is denoted as the driver transition section.

For all computations in this section, a conical body section 2.5 m long with 4.8-mm-thick steel walls is used. In all cases, the exterior geometry of the driver section is a cylinder with diameter 3.5 times that of the explosive charge (for the special case of the conical frustum in Section 3.1, “diameter” refers to the smallest diameter). The interior geometry of the driver housing section corresponds to that of the explosive charge (i.e., cylindrical in all but the frustum case) before immediately transitions to a conical geometry in the driver transition section for mating with the body section of the shock tube. The length of the driver transition section is always taken to be 2 times the charge diameter, and the body section of the shock tube is always 2.5 m long. All computational data in this section are computed at a fixed gauge 2.0 m downstream of the nearest charge surface and off-axis (mainly due to the noise generated on-axis as seen in the previous section). The radial position of the gauges used in this subsection is located halfway between the axis of symmetry and the shock tube wall (i.e., the exact radial location of the gauges depends on the shock tube angle). The length of the tube is taken to extend well beyond the gauge location so that release waves from the exit do not complicate the analysis.

3.1 On the Influence of Driver Section and Charge Design: 10° Conical Shock Tube

The influence of various driver section (e.g., geometry and material) and explosive charge (e.g., geometry and size) modifications on the downstream loading profile is investigated in the following paragraphs. Table 1 lists the computational test matrix used for this investigation, and Fig. 4 depicts a schematic for reference. A 10° cone angle is used for all computations in this subsection. As an example, Fig. 5 shows a zoomed-in view of the ALE3D geometry used for the baseline design, with the design parameters defined in Table 1 for the various iterations.

Table 1 Computational test matrix for 10° shock tube study

Configuration	Driver section material	Backing material	Air gap (mm)	Charge geometry	Charge L/D	Charge diameter (mm)	Charge mass (g)
Baseline	4340 steel	Air	None	Cylinder	1.0	16.0	5.0
50% mass (L/D = 1)						12.7	2.5
50% mass (L/D = 0.5)					0.5	16.0	
150% mass (L/D = 1)					1.0	18.3	7.5
150% mass (L/D = 1.5)					1.5	16.0	
200% mass (L/D = 1)					1.0	20.1	10.0
200% mass (L/D = 2)					2.0	16.0	
L/D = 2						12.7	5.0
Frustum				10° conical frustum	1.25 ^a	16.0	
Air gap			2.0	Cylinder	1.0		
Steel back		32 mm 4340 steel	None				
Al back		32 mm 7075 Al					
Al driver	7075 Al	Air					

^a Measured with respect to the smallest diameter (reported as “charge diameter”)

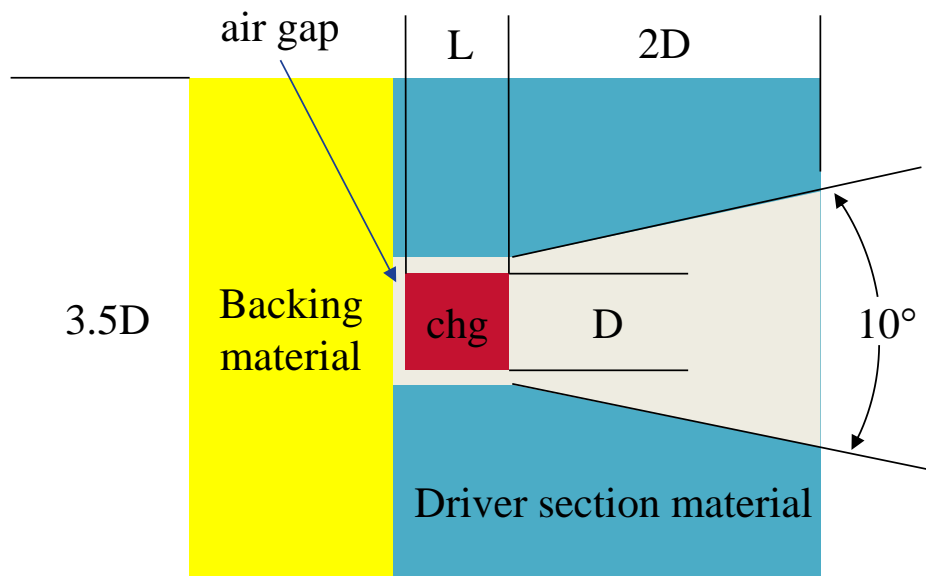


Fig. 4 Schematic of shock tube driver section for reference with Table 1

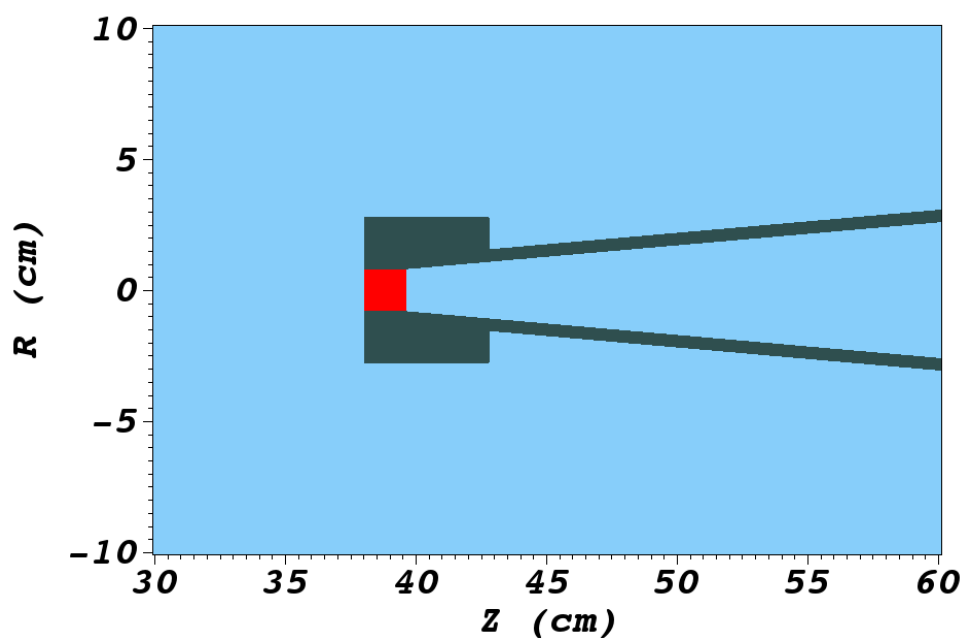


Fig. 5 Zoomed-in view of the ALE3D shock tube entry section geometry for the baseline shock tube design (the red material represents pentolite, the gray represents the steel shock tube, and the blue represents the air)

Figure 6 presents the ALE3D pressure profile for the baseline driver section design with a 5-g driver charge (see Table 1) obtained 2.0 m downstream of the nearest charge surface and halfway between the axis and shock tube wall (approximately 93 mm off-axis for this baseline design). Also included in the figure is the modified Friedlander waveform for a 544-g (1.2-lb) pentolite charge obtained from ConWep (as mentioned in the Introduction, the Friedlander parameters were obtained by inputting ALE3D's peak pressure and distance from the charge to the gauge into ConWep). Notice that the shock tube waveform appears to diverge from the Friedlander around 3.2 ms; this divergence is not due to release waves from the exit of the tube since the shock has only just arrived at the exit, another 0.5 m downstream from the point at which the data is gathered, around 3.2 ms. In general, the loading profile of this baseline case provides a good approximation of a Friedlander waveform.

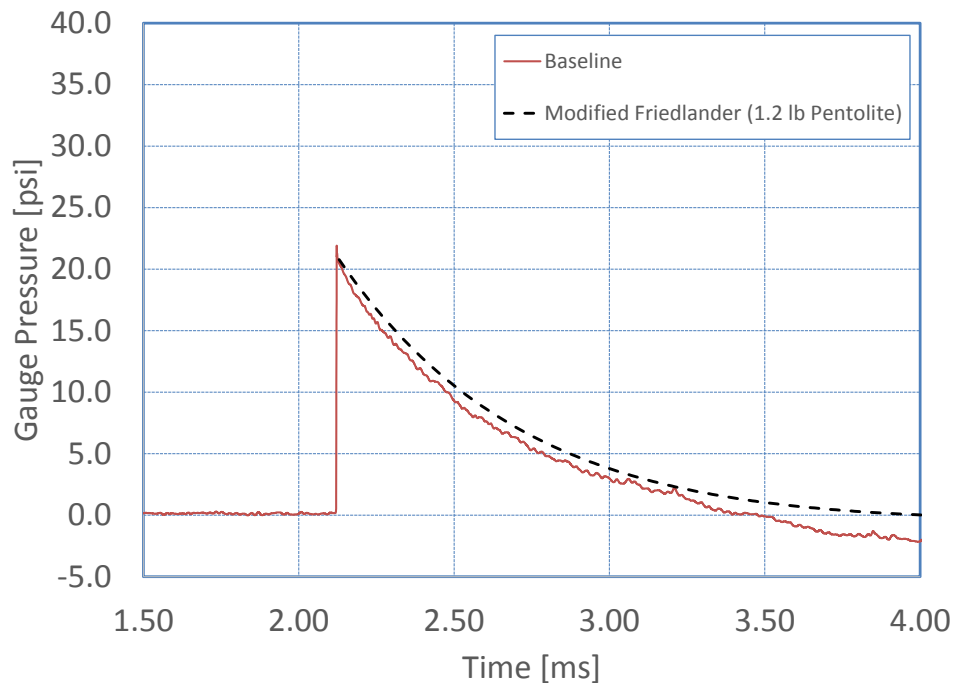
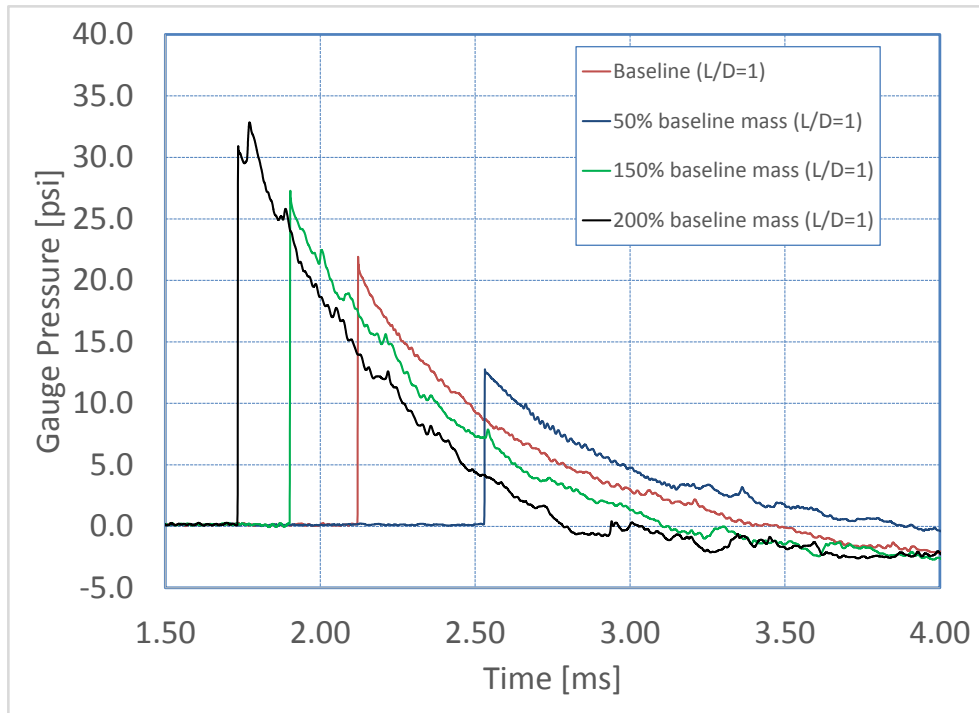
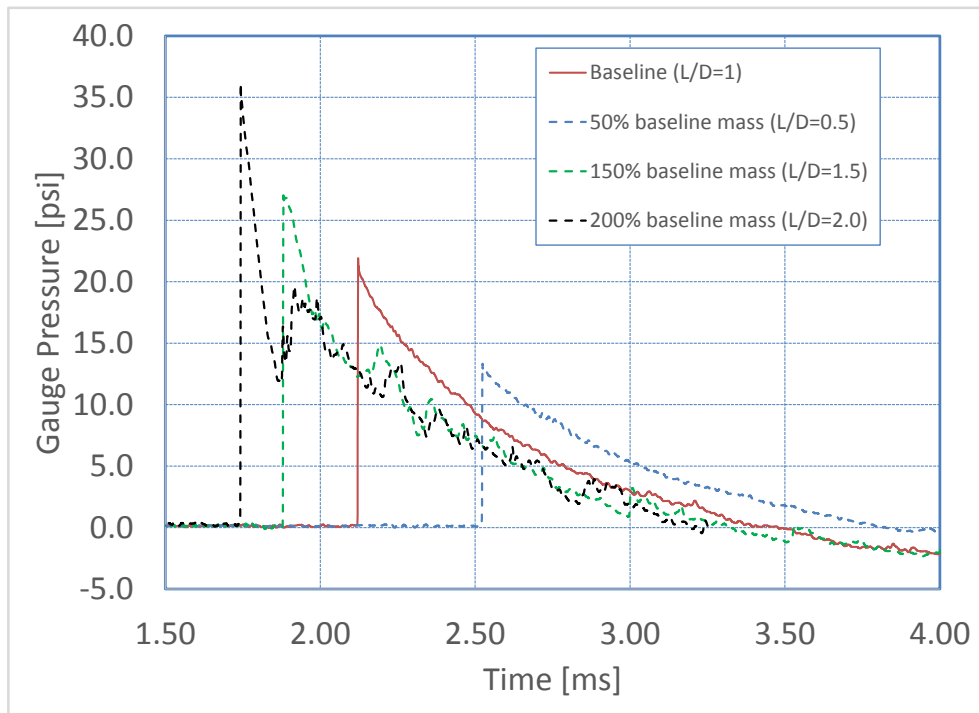


Fig. 6 Pressure loading measured 2.0 m downstream of the driver charge surface for the baseline design of the 10° shock tube driver section and 5-g driver charge compared with a Friedlander waveform obtained from CONWEP for a 544-g (1.2-lb) pentolite charge

Figure 7 shows the resultant air blast as a function of shock tube driver explosive mass. For each mass (other than the baseline), 2 configurations are shown: Fig. 7a shows the aspect ratio being held constant ($L/D = 1$) while the diameter and length are modified, whereas Fig. 7b shows the diameter being held constant ($D = 16.0$ mm) while the charge length is modified. Either configuration results in similar peak pressures relative to the baseline case; however, a comparison of Fig. 7a and Fig. 7b indicates that the longer charges ($L/D > 1$) do a worse job of approximating a Friedlander waveform. For the controlled aspect ratio pressure profiles of Fig. 7a, the peak pressures appear to be increasing at approximately half the rate of the mass (i.e., doubling the mass yields a roughly 50% increase in peak pressure). In general, Fig. 7 indicates that a shock tube with a fixed conical angle is sufficiently flexible to produce a range of loading profiles approximating a Friedlander waveform simply by increasing the explosive mass.



(a)



(b)

Fig. 7 Influence of driver charge mass on the pressure profile of the 10° shock tube measured 2.0 m downstream of the driver charge surface (a) fixed aspect ratio ($L/D = 1$) and (b) fixed charge diameter ($D = 16.0$ mm)

The influence of placing a backing material behind the driver charge is investigated in Fig. 8. In this case, a 32-mm-thick disc of either 4340 steel or 7075 aluminum (Al) is placed directly behind the explosive charge (see Fig. 4) to minimize energy losses due to product gases escaping out the back of the shock tube; the diameters of these backing discs are the same as the outer diameter of the driver section (i.e., 3.5 times the explosive charge diameter). Figure 8 shows that the pressure peak measured at the gauge location 2.0 m downstream from the charge surface is increased substantially (nearly 70% for the steel backing) relative to the baseline case where the product gases freely escape. The Al backing material results in a slightly lower peak pressure relative to using a steel backing material. The shock structure does appear to be significantly noisier when using either Al or steel as a backing material, and the loading profile deviates somewhat from a smooth Friedlander waveform. In fact, the shock profiles when using a backing material other than air (Fig. 8) look qualitatively similar to the shock profiles from having long charges (e.g., the $L/D > 1$ cases in Fig. 7b). One possibility for this similarity is that both designs mitigate the influence of release waves from behind—in the first case due to the relatively high shock impedance backing material and, in the second case, due to the detonation through a relatively longer, narrow channel—and, for similar reasons, generate more secondary shocks in the driver section relative to the baseline case that are then propagated forward down the shock tube body section.

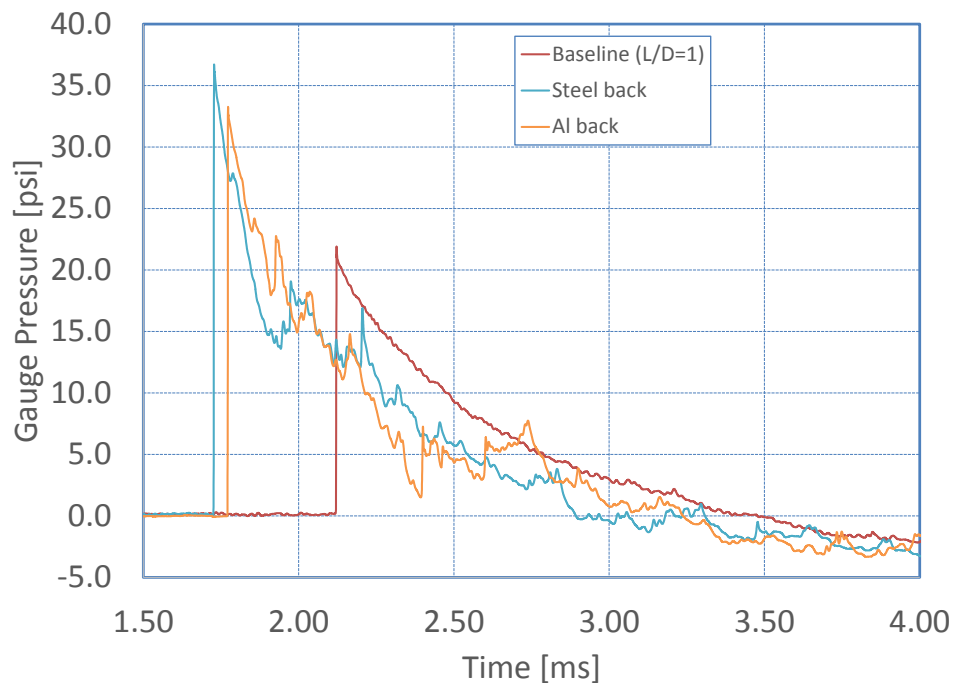


Fig. 8 Influence of a backing plate behind the 5-g driver charge on the pressure profile of the 10° shock tube measured 2.0 m downstream of the driver charge surface

Finally, a number of other modifications, all using a 5-g explosive charge, were investigated and are presented in Fig. 9. Using a frustum geometry for the driver charge (and coincident driver section) instead of the more easily manufactured conical geometry increased the peak pressures by 6%. Introducing an air gap between the explosive and driver section walls also resulted in higher pressures (5.0% higher peak) relative to the baseline. Increasing the charge's L/D from 1 to 2 resulted in a more than 15% decrease in peak pressure relative to the baseline design, while changing the driver section's material from steel to Al decreased the peak pressure by 23.5%. Fabricating the entire shock tube out of Al results in practically the same downstream pressure profile (not shown here) as simply making the driver section Al; this result implies, as might be expected, that the body section primarily serves to propagate the shock waves downstream and does not contribute notably to the downstream pressure profile.

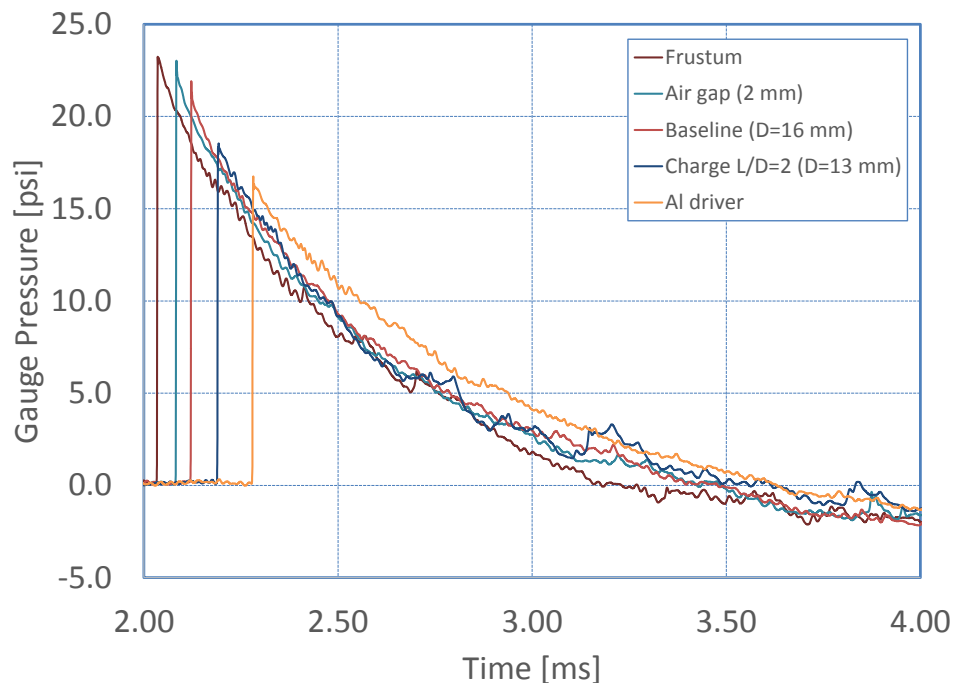


Fig. 9 Influence of various modifications to the driver section and 5-g driver charge on the pressure profile of the 10° shock tube measured 2.0 m downstream of the driver charge surface

One seemingly counterintuitive observation from Fig. 9 is that the introduction of an air gap between the explosive charge and the radial wall of the driver section yields an increase in the downstream pressure relative to the baseline design, which has the explosive charge in contact with the wall. The reasoning for this phenomenon is as follows. The primary blast wave generated when the driver section is in contact with the detonating charge will indeed be slightly stronger than the primary blast wave generated when there is an air gap between the detonating charge and the radial driver section walls; this difference in the primary shock wave

strength is to be expected because of release waves at the explosive-air interface when an air gap is present. However, there are also reflected shock waves that are generated behind the detonation wave, some of which combine downstream with the primary blast wave generated from the detonation front, and it is this combined shock wave that is measured downstream.

When the driver section wall is in contact with the detonating charge, reflected shock waves are generated at the wall-explosive interface (and transmitted back through the product gases) from the velocity component of the curved detonation wave that is normal to the radial wall; much of these reflections get lost out the open end of the shock tube into the surrounding air. In contrast, when an air gap is introduced between the explosive charge and the wall of the driver section, release waves decrease the pressures at the explosive's radial surface, as would be expected, but the impact of the expanding product gases with the wall generates a reflected shock wave back through the explosive products (see the top half of Fig. 10), which then gets transmitted downstream and eventually combines with the primary air blast. The shock waves reflected back into the product gases when an air gap is present are moving toward the axis and down the shock tube because of the direction of the expanding gases when they impact and, therefore, fewer of these shock waves are lost out of the open end of the shock tube. In either case, the secondary shock reflection (and subsequent reflections off the axis and shock tube wall) gets transmitted into the air downstream and eventually combines with the primary air blast because of the detonation wave.

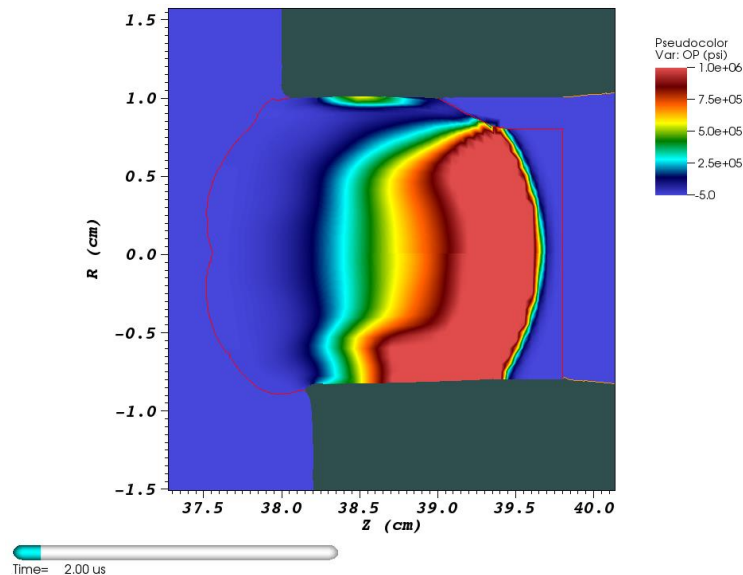


Fig. 10 Pressure contours at 2 μ s after detonation showing the detonation wave and shock reflections through the explosive driver charge (red boundary line) for the baseline case with no air gap between the driver charge and the steel walls (bottom half) and for the case with a 2-mm air gap (top half)

Table 2 lists the peak overpressures for all cases investigated in this subsection (see also Table 1) and the percent difference of these peak pressures relative to the baseline. Using a steel backing disc in the driver section resulted in the highest peak pressure relative to the baseline (higher even than doubling the explosive mass), whereas using an Al driver or halving the explosive mass resulted in the lowest peak pressures.

Table 2 Peak pressures (gauge) in 10° shock tube study

Configuration	Charge mass (g)	Peak overpressure @ 2 m (psi)	% diff from baseline
Baseline	5.0	21.92	0.0
50% mass (L/D = 1)	2.5	12.77	-41.7
50% mass (L/D = 0.5)		13.33	-39.2
150% mass (L/D = 1)	7.5	27.29	24.5
150% mass (L/D = 1.5)		27.02	23.3
200% mass (L/D = 1)	10.0	32.85	49.9
200% mass (L/D = 2.0)		36.14	64.9
L/D = 2	5.0	18.54	-15.4
Frustum		23.23	6.0
Air gap		23.02	5.0
Steel back		36.72	67.6
Al back		33.27	51.8
Al driver		16.76	-23.5

3.2 On the Influence of Cone Angle

Section 3.1 focuses on the influence of various modifications to a 10° conical shock tube. In this subsection the influence of cone angle will be investigated. The baseline design from the previous subsection will be used in this section as well: in other words, a cylindrical explosive charge, $L/D = 1$, no air gap, a steel driver section, and no backing material. Table 3 provides a computational test matrix for the ALE3D calculations performed in this subsection.

Table 3 Computational test matrix for shock tube cone angle study

Cone angle (°)	Ideal performance factor	Estimated performance factor ^a	Shock tube driver charge (g)
10	526	109	5
20	132	27	20
30	59	12	45
40	33	6.8	80
50	21	4.4	123

^a Assuming 20.7% efficiency based on comparing 10° ALE3D calculations with CONWEP.

A shock tube's performance factor is defined as the equivalent free-field mass divided by the shock tube's explosive mass. The equivalent free-field mass is the explosive mass that, when detonated in the free-field, is necessary to achieve similar pressures and impulses at the gauge or test location to those measured in the shock tube. This equivalent mass can be determined using free-field experiments or estimated using computational tools; in this report, the equivalent mass is estimated using ConWep. The ideal performance factor, PF_I , for a conical shock tube is found as in Stewart and Pecora (2015) from the following equation:

$$PF_I = \frac{2}{1 - \cos\left(\frac{\theta}{2}\right)}, \quad (2)$$

where θ is the full cone angle (for example, $\theta = 10^\circ$ in Fig. 4).

The efficiency of the shock tube is defined as the actual performance factor divided by the ideal performance factor from Eq. 2. In this section, an estimate of the actual performance factor is found by considering the 5-g charge in the 10° shock tube and comparing the pressure load at 2.0 m with an equivalent free-field air blast from ConWep. In the case of the baseline 10° shock tube design, this procedure results in an estimate of 20.7% efficiency. If it is assumed (without justification) that the shock tube efficiency is constant with cone angle, then the estimated performance factors shown in Table 3 are arrived at, and the masses of the shock tube explosive

charges required to approximate the air blast from a 544-g (1.2-lb) free-field pentolite charge can be determined.

Figure 11 shows the air blast profile 2.0 m downstream for the baseline 10° shock tube presented in the previous subsection (see, for example, Fig. 6) along with results from the different cone angles of Table 3. All waveforms are taken at radial locations off the axis of symmetry and halfway between the axis and the shock tube wall (i.e., the gauge's axial location is always 2.0 m downstream, but the radial location depends on the cone angle). The waveforms of both the 10° and 20° conical shock tubes do a reasonable job of approximating a Friedlander waveform; however, the shock tubes with cone angles of 30° and above indicate multiple strong shocks in the flow field (see also Fig. 12), which is not desirable if the goal is to approximate the Friedlander waveform seen in free-field air blast experiments. Unfortunately, these trailing shocks behind the primary air blast show up in the flow field regardless of modifications to the driver section or driver charge (i.e., making modifications similar to what was investigated in the previous subsection as well as using a planar detonation instead of a point detonation). This presence of strong secondary shocks downstream and the general nonuniformity of the flow field shown in Fig. 12b, regardless of driver section/charge design, indicate that when increasing the cone angle, there may be a critical angle at which the flow cannot stay attached to the shock tube walls.

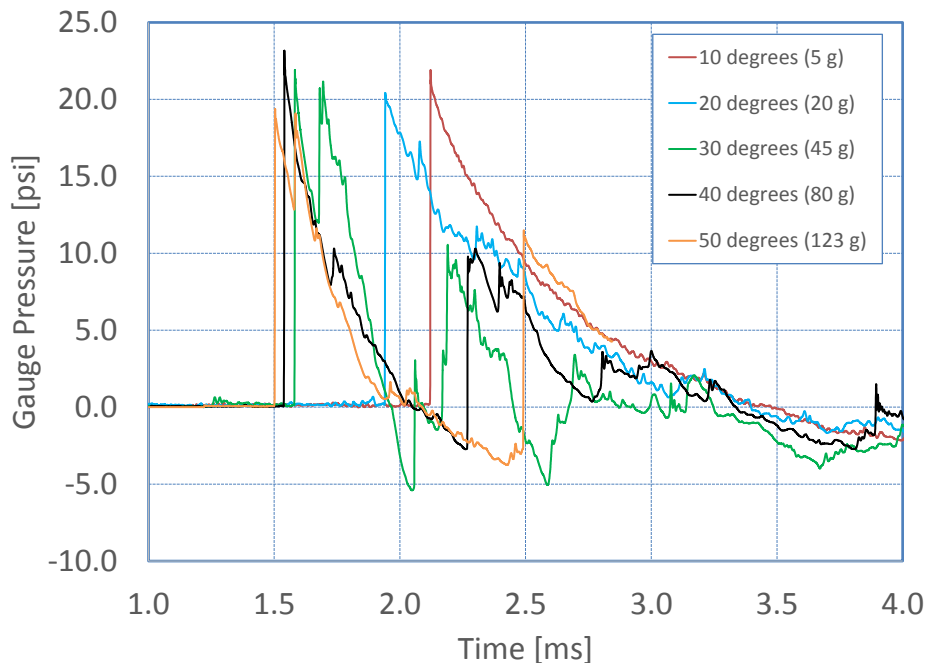
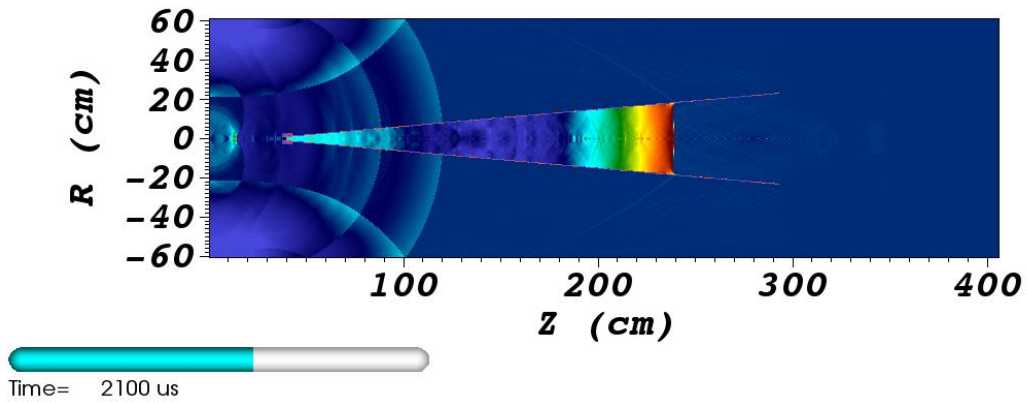
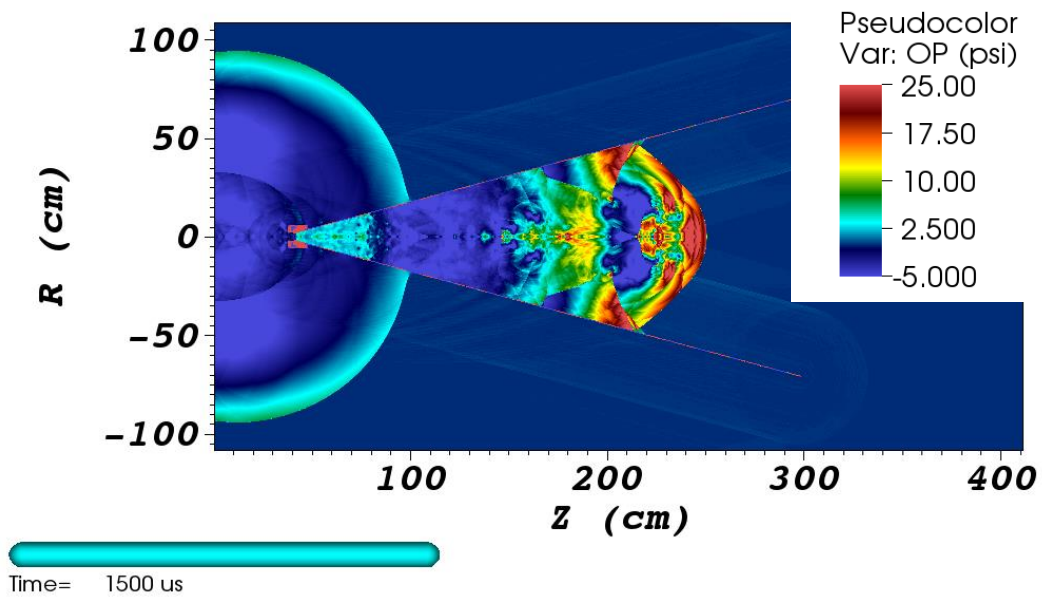


Fig. 11 Influence of shock tube cone angle on the pressure profile measured 2.0 m downstream of the driver charge surface



(a)



(b)

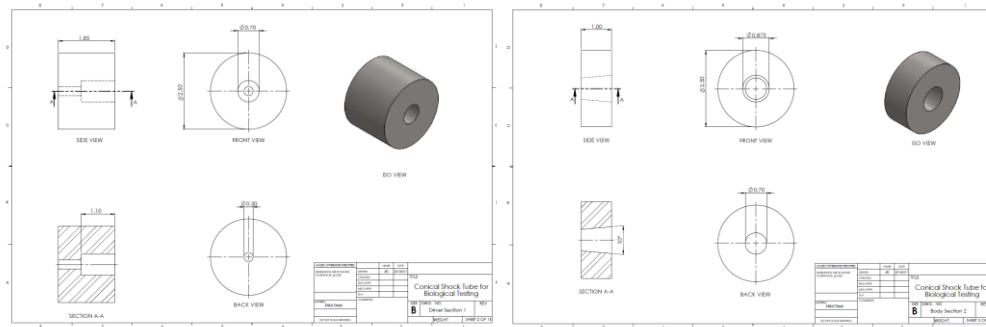
Fig. 12 Comparison of pressure contours at the approximate times when the primary blast wave has traveled 2.0 m inside the shock tube: (a) 10° cone (2.1 ms) and (b) 30° cone (1.5 ms)

4. 10° Shock Tube: Computational and Experimental Results

This section documents the resulting air blast from a 10° conical shock tube, which uses a driver section design that blends various features (e.g., air gap, steel back, $L/D = 2$) investigated in Section 3.1. This driver section was fabricated prior to completing the computational study presented in Section 3.1 and is likely not an ideal design; however, the experimental series provides data for comparison with the computational trends discussed in the previous section. The current section is

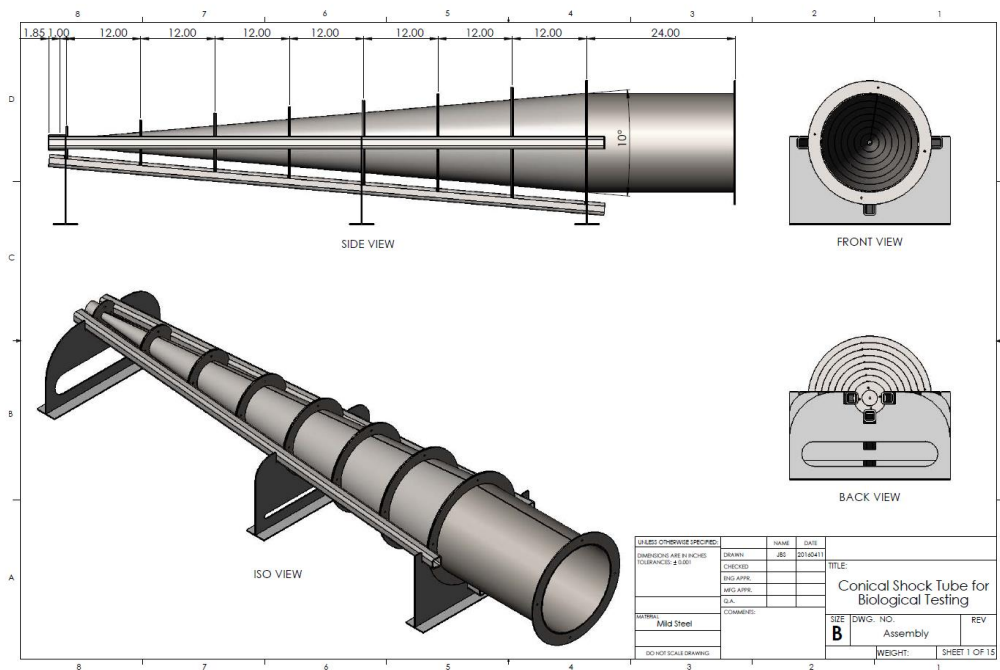
structured as follows. Section 4.1 presents a comparison of ALE3D computational data with experimental data obtained using PCB Piezotronics 50-psi blast pencil gauges placed at various locations downstream of the explosive charge and either on the axis of the shock tube or 101.6 mm (4 inches) off axis. Section 4.2 then investigates the use of a cylindrical exit section to alleviate the release wave interaction with the blast wave at the exit of the cylindrical shock tube body section. Only selected experiments will be presented in the current section. Data from additional experiments can be found in the Appendix.

Basic engineering drawings for the shock tube used to collect the experimental data in this section are shown in Fig. 13. The shock tube is fabricated from mild steel throughout. The driver section has a 19.05-mm-thick steel disc backing the 5-g pentolite charge, which is separated from the steel walls (both back and radial) by a 2.54-mm-thick foam centering device. A 7.62-mm hole is drilled through both the steel back and the foam centering device to allow for insertion of the RISI RP-80 detonator. The outer diameter of the driver section is 63.5 mm, and the inner diameter at the smallest end is 17.78 mm. The explosive charge used throughout is 12.7 mm in diameter and 25.4 mm long. The driver transition section (Fig. 13b) extends 25.4 mm beyond the surface of the charge, which sits flush with the end of the driver housing section. The body section of the tube (Fig. 13c) is 4.76 mm thick and comprises seven 304.8-mm-long conical sections; the inner diameter at the exit of the shock tube (i.e., at the end of the seventh conical section) is 395.6 mm. Some of the experiments include a 609.6-mm-long cylindrical exit section to alleviate release waves at the exit of the conical section. In all figures, “exit” denotes the exit of the shock tube’s body section (i.e., 2.16 m downstream from the nearest surface of the 5-g explosive charge), regardless of whether an exit section is attached.



(a)

(b)



(c)

Fig. 13 Shock tube basic engineering drawings (dimensions are in inches): (a) driver housing section, (b) 10° conical driver transition section, and (c) 10° conical body section including the cylindrical exit section

4.1 Computational Predictions vs Experimental Results

The first set of experiments were conducted without the cylindrical exit section, as shown in Fig. 14. The shock tube was placed on top of a steel frame that was attached to a 152.4-mm (6-ft)-tall wooden stand. This stand was designed to avoid the influence of shock waves reflecting off the ground and interacting with the air blast.

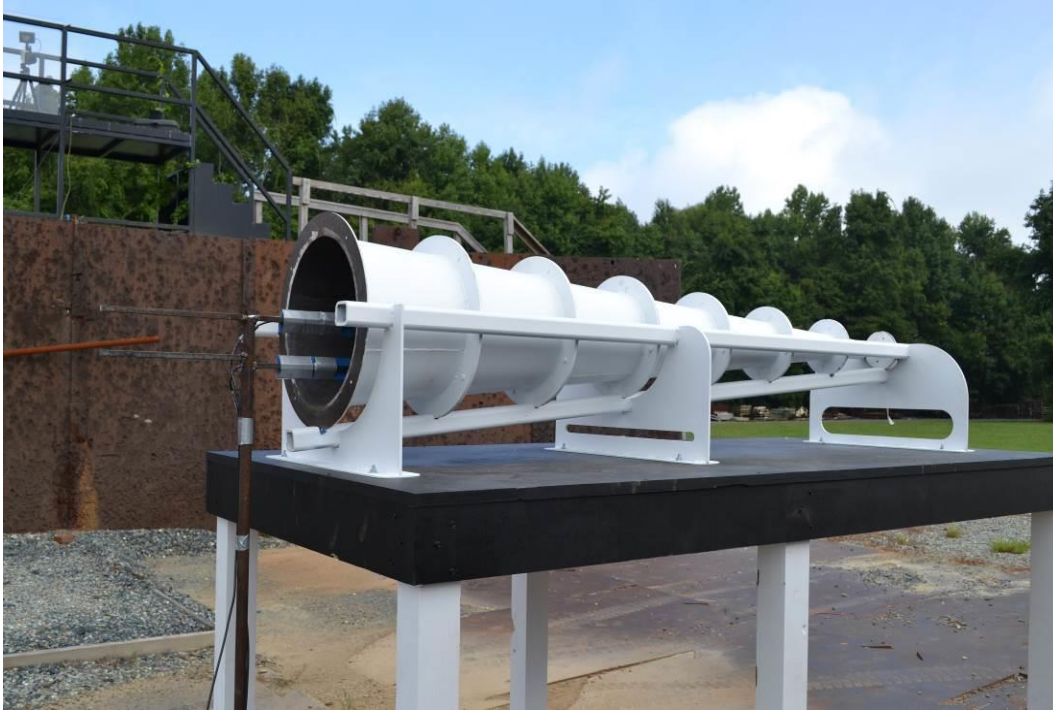


Fig. 14 10° shock tube, without the cylindrical exit section

The shock tube's driver section is shown in Fig. 15. Figure 15a shows the 5-g pentolite charge (white cylinder), foam centering device (light blue), cylindrical portion that houses the explosive charge inside the centering device (see also Fig. 13a), and the conical transition section (see also Fig. 13b) that mates up with the conical body section of the shock tube prior to conducting one of the experiments. Figure 15b shows the driver section after an experiment has been conducted, indicating some minor deformation of the steel adjacent to the detonated explosive. A new driver section (both the cylindrical and transition portions) was used for each experiment conducted in this series.



(a)

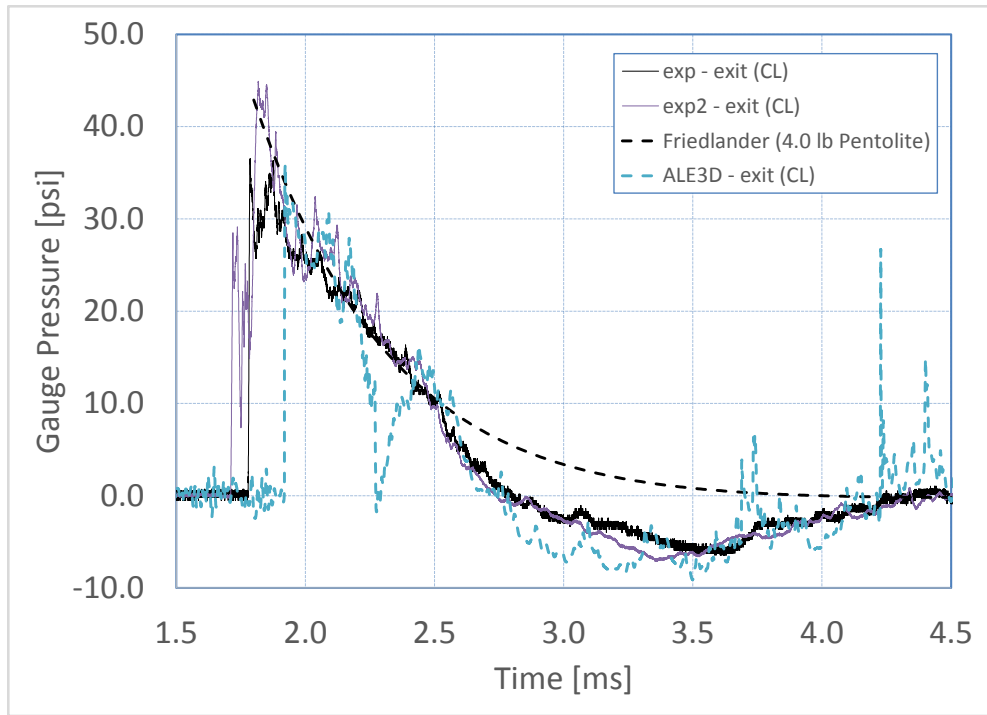


(b)

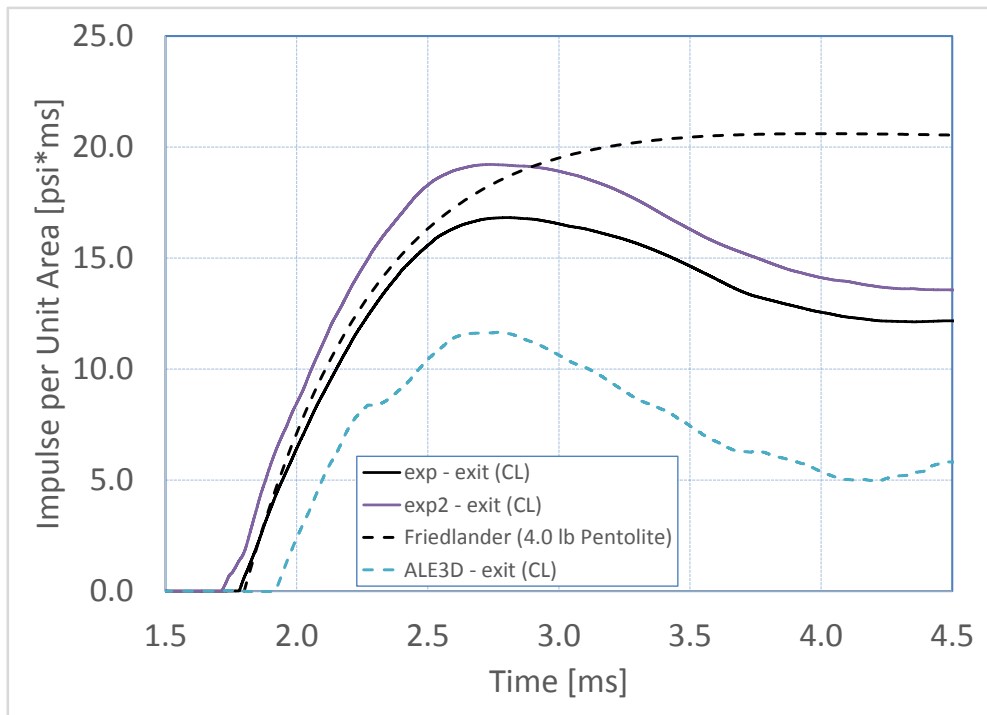
Fig. 15 Example shock tube driver section used in an experiment: (a) (from left to right) pentolite explosive charge, blue foam centering device, cylindrical driver housing section, and conical driver transition section prior to the experiment; (b) driver housing section and driver transition section postexperiment

The blast profiles from 2 separate experiments where the pencil gauges are placed at the exit of the shock tube's conical body section are shown in Figs. 16 and 17. Pencil gauges were placed both on-axis (denoted "CL" in Fig. 16) as well as 101.6 mm (4 inches) off-axis (denoted "OA" in Fig. 17). Figures 16a and 17a show a comparison between the pressure time histories of the experimental data with both ALE3D computational data (the pentolite density is taken to be 1.69 g/cm^3 , consistent with experimental estimates) and a Friedlander waveform. For these shock tube experiments, the pressure peak and initial decay of the air blast are described well by the Friedlander waveform corresponding to a 1814-g (4-lb) sphere of pentolite. This result translates to a performance factor (i.e., actual charge mass/effective charge mass) of roughly 360 compared to the performance factor of 60 obtained with the earlier 17° shock tube (see Section 2). Figures 16b and 17b show the corresponding impulse per unit area obtained by integrating the pressure profile over time. A few things are evident from Figs. 16 and 17:

- The experimental peak overpressures and impulses are significantly higher than those obtained using ALE3D, and the agreement is notably worse than that obtained using the air-backed driver section in the 17° tube (see Figs. 2 and 3).
- The experimental pressure profiles indicate a far less uniform shock front and overall structure relative to either the ALE3D predictions or the earlier 17° shock tube results shown in Figs. 2 and 3.
- The experimental data do a reasonable job of reproducing a Friedlander waveform, especially in terms of the impulses, until release waves arrive (at approximately 2.5 ms), at which point the pressures and impulses rapidly decay relative to the Friedlander waveform.

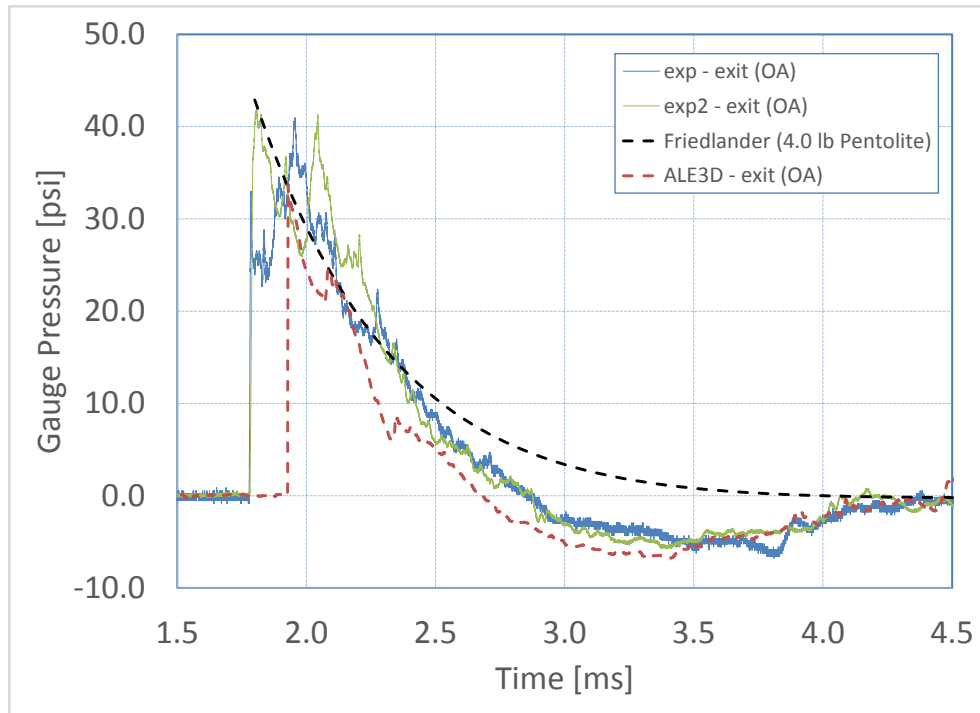


(a)

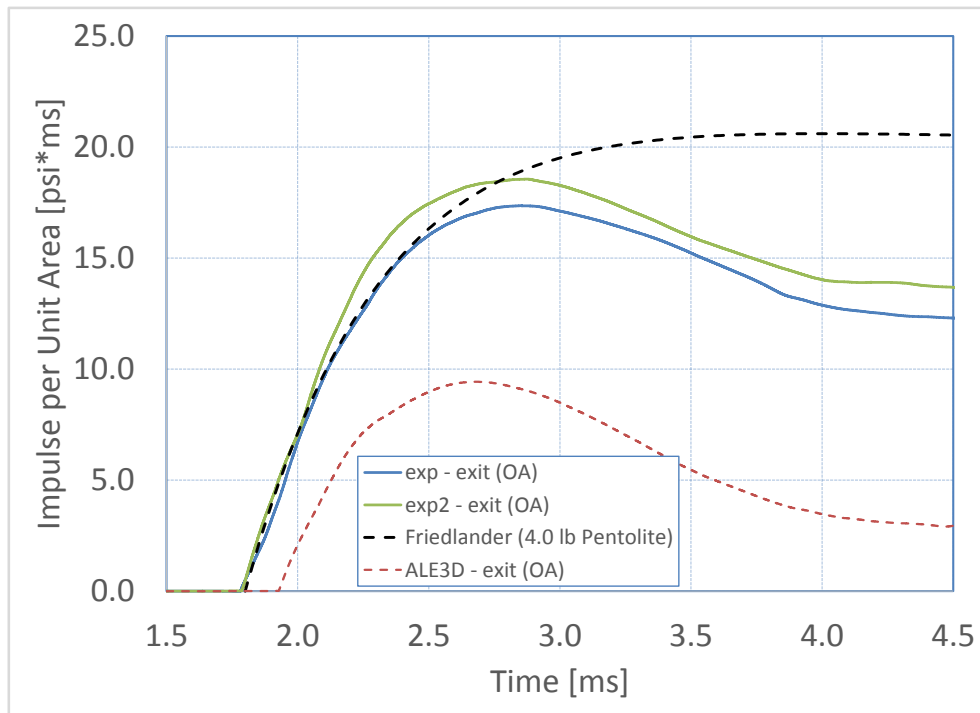


(b)

Fig. 16 Comparison of experimental vs computational data on the axis of symmetry and at the exit (2.16 m from the nearest surface of the pentolite explosive driver charge) of a 10° shock tube: (a) overpressure and (b) impulse per unit area



(a)



(b)

Fig. 17 Comparison of experimental vs computational data 10 cm off the axis of symmetry and at the exit (2.16 m from the nearest surface of the pentolite explosive driver charge) of a 10° shock tube: (a) overpressure and (b) impulse per unit area

One possible explanation for the first 2 observations listed previously (i.e., that the 10° shock tube experimental data and ALE3D computational data agree much less than in the previous 17° shock tube results summarized in Section 2) is that the pentolite JWL model is simply less accurate compared to the C4 JWL model used previously (there are no cylinder expansion data for the pentolite at the assumed density of 1.69 g/cm³). Additionally, as mentioned in Section 3.1, the steel backing material results in a shock being reflected back into the compressed product gases, and this re-shock of the product gases may be difficult for the JWL model to accurately capture. This re-shock issue is an especially plausible culprit since the 50% TNT in pentolite is known to behave non-ideally (i.e., there could be secondary reactions occurring in the experiments due to re-shocks—reactions that the model is not calibrated to capture). A third potential explanation for the first 2 observations is that the under-resolved mesh being used in this study (see the discussion in the Introduction) provides a worse approximation of the 10° shock tube's performance relative to the 17° case. A degraded approximation could be due to, for example, either the relatively fewer elements across the radius of the explosive charge (a 5-g charge was used for the 10° tube compared to a 14.5-g charge in the 17° case) or the increased influence of the shock tube walls in the smaller angle case.

4.2 Mitigation of Release Waves at the Exit Section

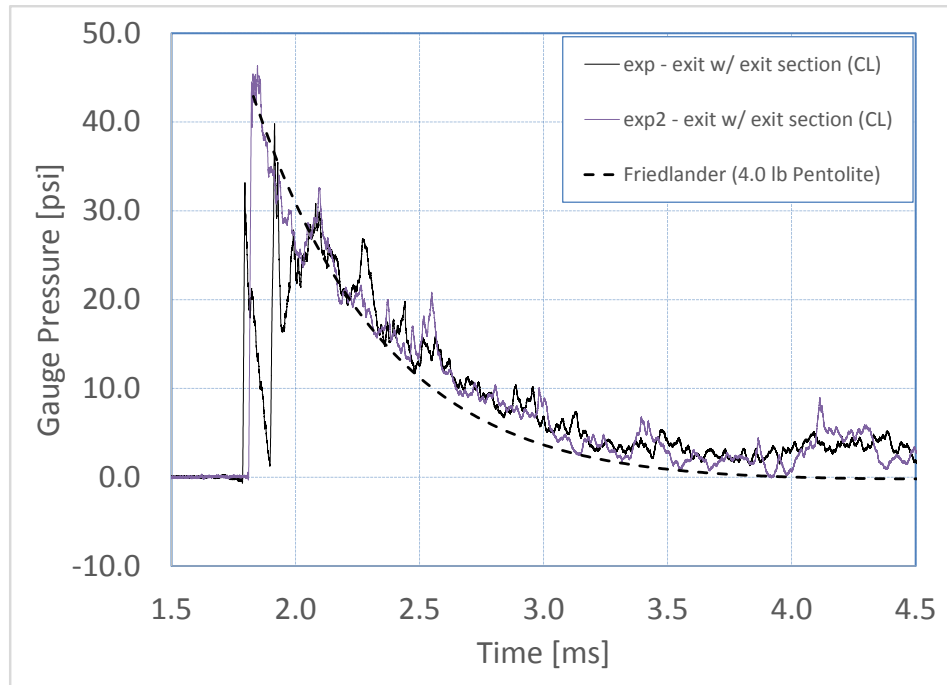
One observation from the shock tube experimental data in Figs. 16 and 17 relative to the Friedlander waveform is that release waves arriving radially from the shock tube exit have a significant influence on the shock tube blast profile (these release waves were also evident in the earlier shock tube work presented in Figs. 2 and 3). This release wave interaction prevents the shock tube blast profile from providing a reasonable approximation of an air blast resulting from a free-field detonation once the release waves interact with it. There are 2 obvious ways to alleviate the influence of the release waves: 1) insert the test item far enough up the shock tube that the release waves do not arrive to influence the experiment during the time period of interest, or 2) extend the shock tube.

In this subsection, the second approach is taken by attaching a 609.6-mm (2-ft) cylindrical exit section to the conical shock tube (see Fig. 18). Ideally, the geometry of the exit section would be a rectangular prism so that windows could be straightforwardly inserted for optical diagnostics. However, this cylindrical geometry is a first step toward developing a test section that both alleviates the influence of release waves and allows for easier integration of diagnostics.

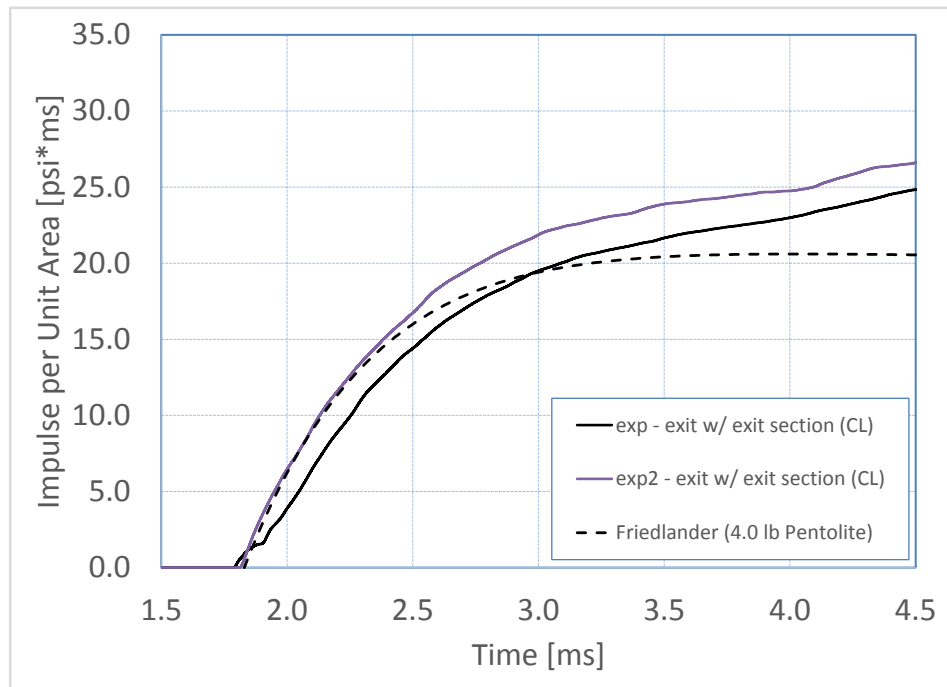


Fig. 18 10° shock tube, with the cylindrical exit section attached

Figures 19 and 20 show the experimental data on- and off-axis, respectively, when using the cylindrical exit section compared with the same Friedlander waveform from Section 4.1 (i.e., due to an 1814-g pentolite free-field detonation). It is evident when comparing the blast profiles with the cylindrical exit section in Figs. 19 and 20 with the profiles shown in Figs. 16 and 17 without an exit section that the prevention of release waves leads to better agreement with the Friedlander free-field air blast. Unfortunately, the blast profiles when using a cylindrical exit section result in greater impulses relative to the Friedlander waveform and impulses that continue to increase beyond the time where the Friedlander has peaked. Both of these features are likely due to the fact that the air blast is being constrained by a constant rather than a diverging geometry once it leaves the shock tube's conical body section and enters into the cylindrical exit section.

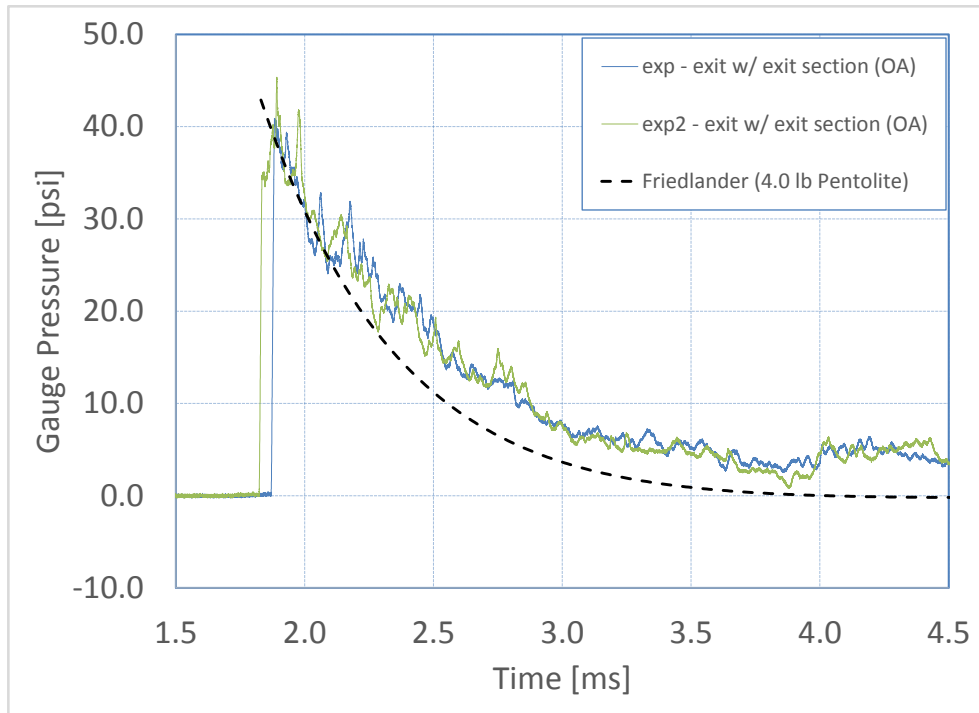


(a)

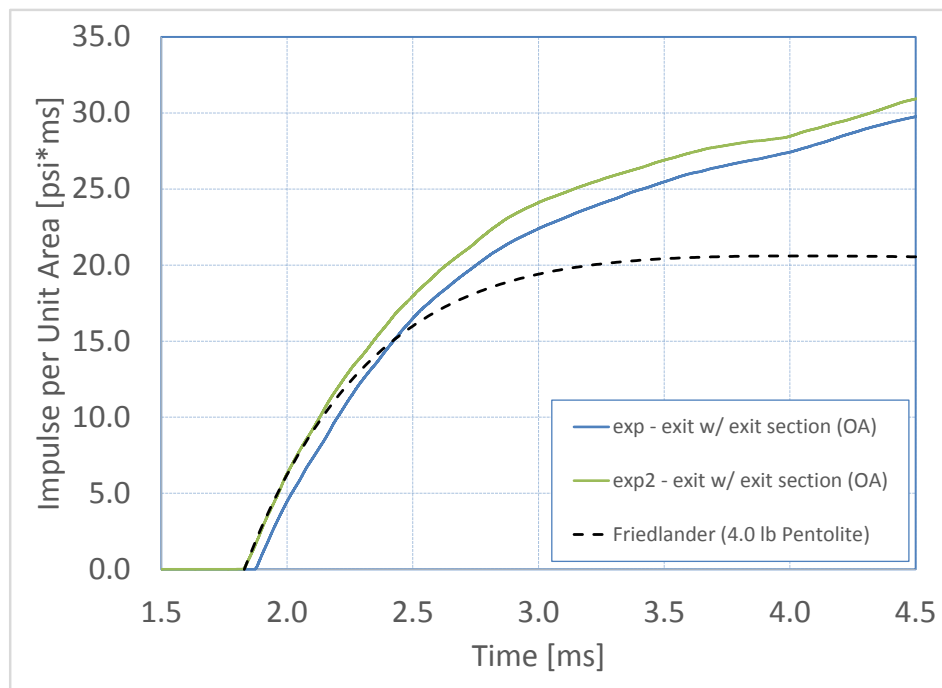


(b)

Fig. 19 Comparison of experimental data on the axis of symmetry and at the exit (2.16 m from the nearest surface of the 5-g pentolite explosive driver charge) of a 10° shock tube with an exit section vs a Friedlander waveform: (a) overpressure and (b) impulse per unit area



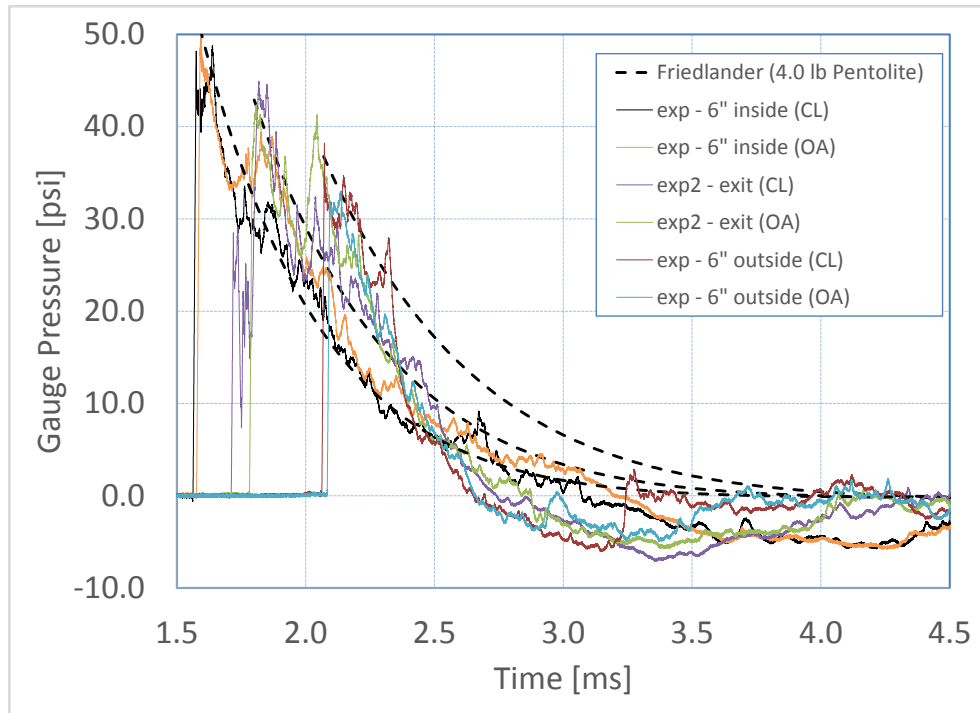
(a)



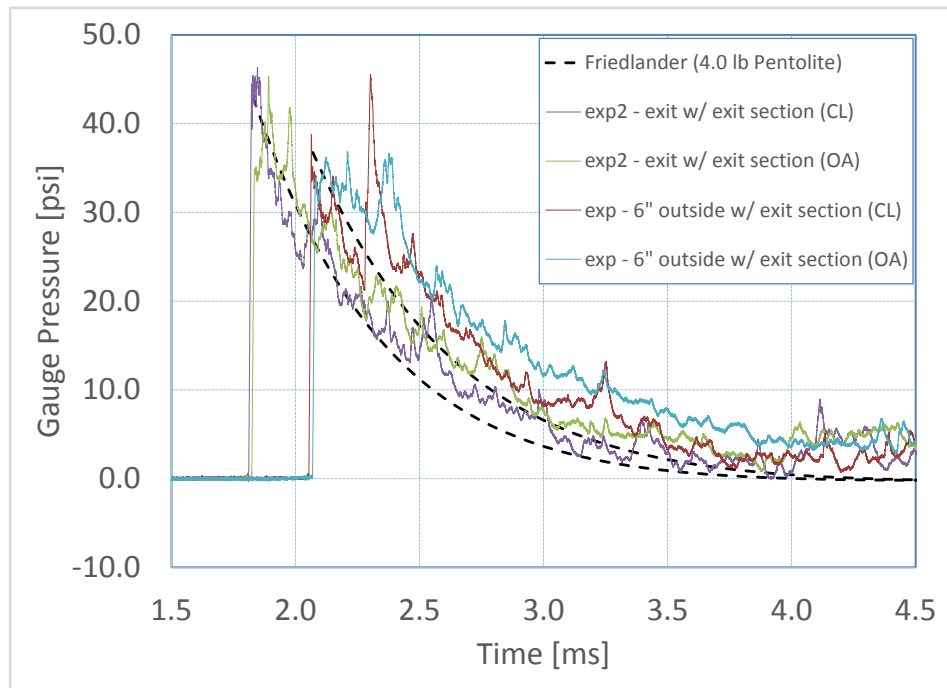
(b)

Fig. 20 Comparison of experimental data 10 cm off the axis of symmetry and at the exit (2.16 m from the nearest surface of the 5-g pentolite explosive driver charge) of a 10° shock tube with an exit section vs a Friedlander waveform: (a) overpressure and (b) impulse per unit area

Figure 21 shows shock tube experimental data using the 5-g pentolite driver charge versus the Friedlander waveform due to an 1814-g pentolite free-field detonation for the configuration with no exit section (Fig. 21a) and using an exit section (Fig. 21b). Obviously, the exit section alleviates the influence of release waves. When using the exit section, there appears to be a secondary shock reflected into the exit section (see, for example, the outside curves in Fig. 21b around 2.3 ms). This secondary shock is likely due to a reflection off the cylindrical steel walls when the slope changes from the conical section to the cylindrical section. It is possible that this shock reflection could be mitigated by using a material with a lower shock impedance than the steel being used in this work. In general, the use of an exit section shows promise for alleviating the release wave interactions with the air blast exiting the conical body section of the shock tube.



(a)



(b)

Fig. 21 Shock tube experimental air blast data due to a 5-g pentolite charge at various locations compared with the Friedlander waveforms at corresponding locations for an 1814-g pentolite charge: (a) without an exit section and (b) with an exit section

5. Conclusions

This report has detailed both computational and experimental work focused on the design of explosively driven conical shock tubes. Earlier experimental work done by the author using a 17° shock tube was compared with ALE3D computational data to demonstrate the ability of the computations to capture the main features of interest (e.g., the pressure loading profiles and impulse per unit area). This computational approach was then used to conduct a parametric study on various shock tube design parameters, such as cone angle and explosive driver geometry. The study was conducted to investigate the influence of these parameters on the air blast 2.0 m downstream of the explosive charge and to determine shock tube driver modification options that might be used to tailor the air blast arriving downstream at a test location. Experimental data from a 10° shock tube utilizing various features from the computational parametric study was presented and compared with ALE3D predictions. This same shock tube was also employed with a newly designed exit section to successfully alleviate the influence of release waves on the measured air blast.

The 10° shock tube resulted in a much higher performance factor than the earlier 17° shock tube (roughly 360 instead of the earlier 60, as calculated using modified Friedlander curves taken from ConWep). However, 2 issues arose out of the experimental work with the 10° conical shock tube: 1) the experimental data were much noisier using the 10° shock tube than the data collected using the previous 17° shock tube, and 2) the ALE3D computational approach provided a much worse comparison to the 10° shock tube experimental data than it did to the earlier 17° shock tube experimental data. Both issues can potentially be explained by the presence of the steel back used in the 10° shock tube compared with the open back used in the 17° shock tube. The steel back results in an increase in reflected shock waves being transmitted into the compressed product gases that eventually propagate downstream. These secondary shock waves could result in the noisy signals observed when using the 10° tube relative to the 17° tube. It is also possible that the reflected shock waves promote secondary reactions in the pentolite (pentolite is 50% PETN and 50% TNT, the latter of which is known to behave in a nonideal manner)—reactions that are not captured by the simple JWL model being employed in the calculations.

One option that will be investigated in the future is the use of a driver section without a steel backing disc in the 10° shock tube to see if 1) the pressure loading profiles become less noisy relative to the experimental data presented here and 2) if the inability of the ALE3D computational data to replicate the experimental results is due to problems associated with shock reflections off the steel back plate.

6. References

- Courtney AC, Andrusiv LP, Courtney MW. Oxy-acetylene driven laboratory scale shock tubes for studying blast wave effects. *Review of Scientific Instruments*. 2012;83(4):045111.
- Dewey JM. The shape of the blast wave: studies of the Friedlander equation. *Proceedings of the 21st International Symposium on Military Aspects of Blast and Shock*; 2010; Jerusalem, Israel.
- Freidlander FG. The diffraction of sound pulses. I. Diffraction by a semi-infinite plate. *Proc Roy Soc Lond A*. 1946;186:322–344.
- Henshall BD. On some aspects of the use of shock tubes in aerodynamic research. London (UK): Aeronautical Research Council Reports and Memoranda, Her Majesty's Stationary Office; 1957. R & M No. 3044.
- Hyde DW. Microcomputer programs CONWEP and FUNPRO, applications of TM 5-855-1, fundamentals of protective design for conventional weapons (user's guide). Vicksburg (MS): Army Corps of Engineer Waterways Experiment Station Structures Lab; 1988. Report No.: WES/IR/SL-88-1.
- Nichols AL III. An arbitrary Lagrange/Eulerian 2D and 3D code system. Ver. 4.24.x. Livermore (CA): Lawrence Livermore National Laboratories; 2014 Sep. Report No.: LLNL-SM-662355; Vols. 1 and 2.
- Stewart JB, Pecora C. Explosively-driven air blast in a conical shock tube. *Review of Scientific Instruments*. 2015;86(3):035108.

Appendix. 10° Shock Tube Pencil Gauge Data

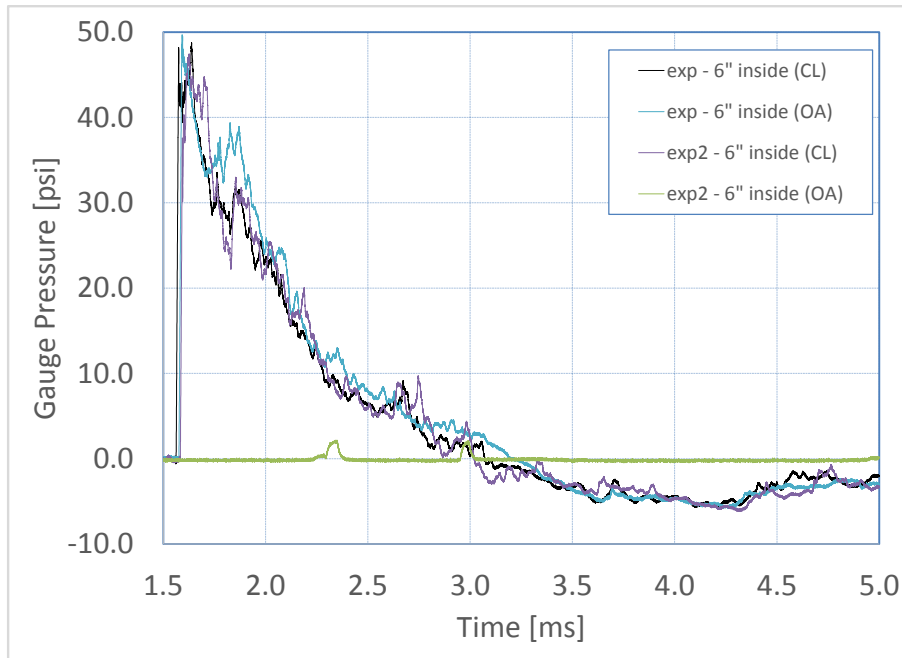


Fig. A-1 Experimental data from pencil gauges inserted 6 inches inside the shock tube's conical exit (i.e., 2.00 m from the charge surface), with no cylindrical exit section. Data are shown from 2 experiments, both on and 102-mm off-axis.

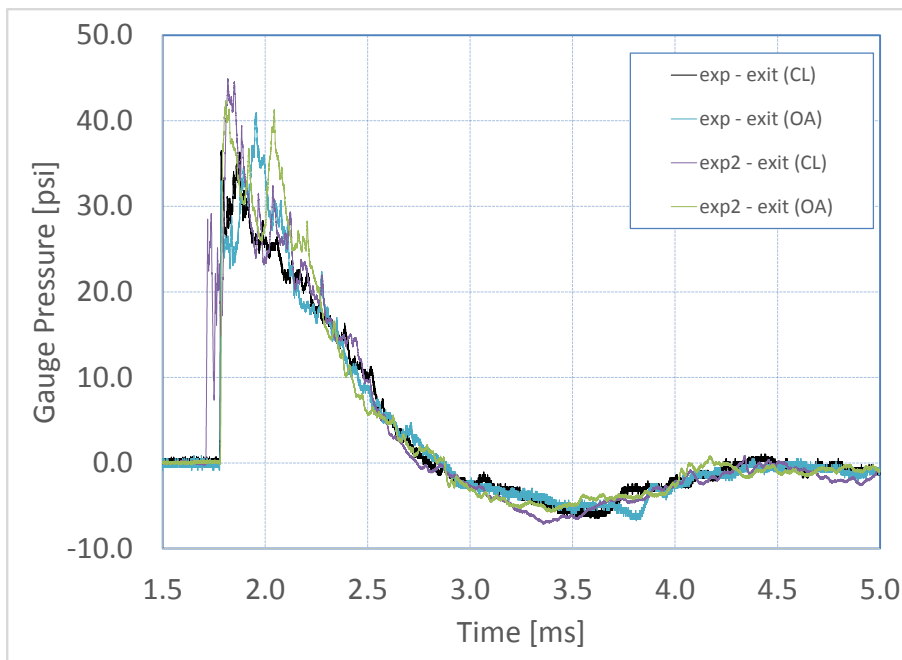


Fig. A-2 Experimental data from pencil gauges inserted at the shock tube's conical exit (i.e., 2.16 m from the charge surface), with no cylindrical exit section. Data are shown from 2 experiments, both on and 102-mm off-axis.

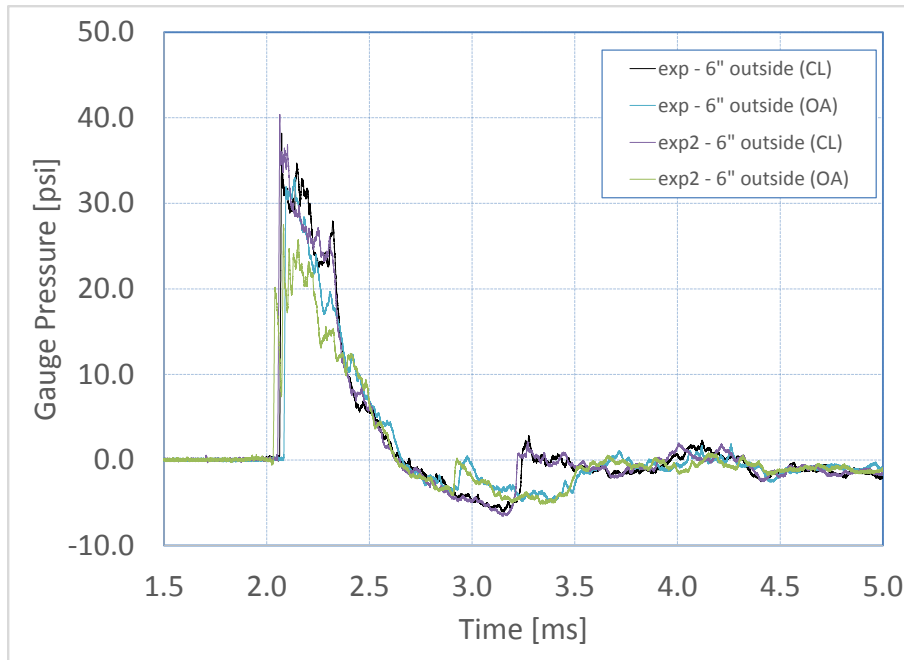


Fig. A-3 Experimental data from pencil gauges inserted 6 inches outside the conical shock tube's exit (i.e., 2.31 m from the charge surface), with no cylindrical exit section. Data are shown from 2 experiments, both on and 102-mm off-axis.

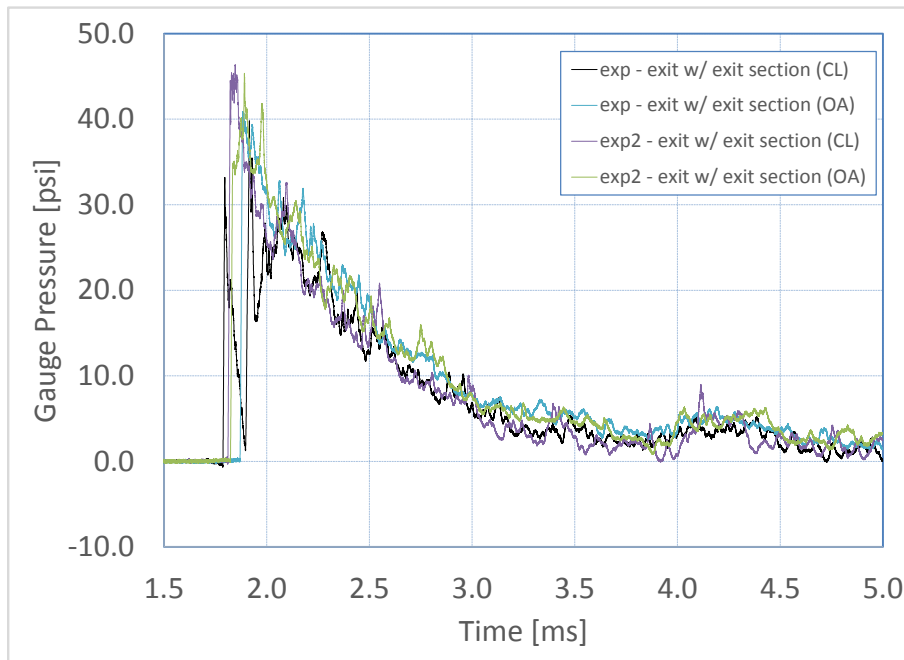


Fig. A-4 Experimental data from pencil gauges inserted at the shock tube's conical exit (i.e., 2.16 m from the charge surface), when a cylindrical exit section is used. Data are shown from 2 experiments, both on and 102-mm off-axis.

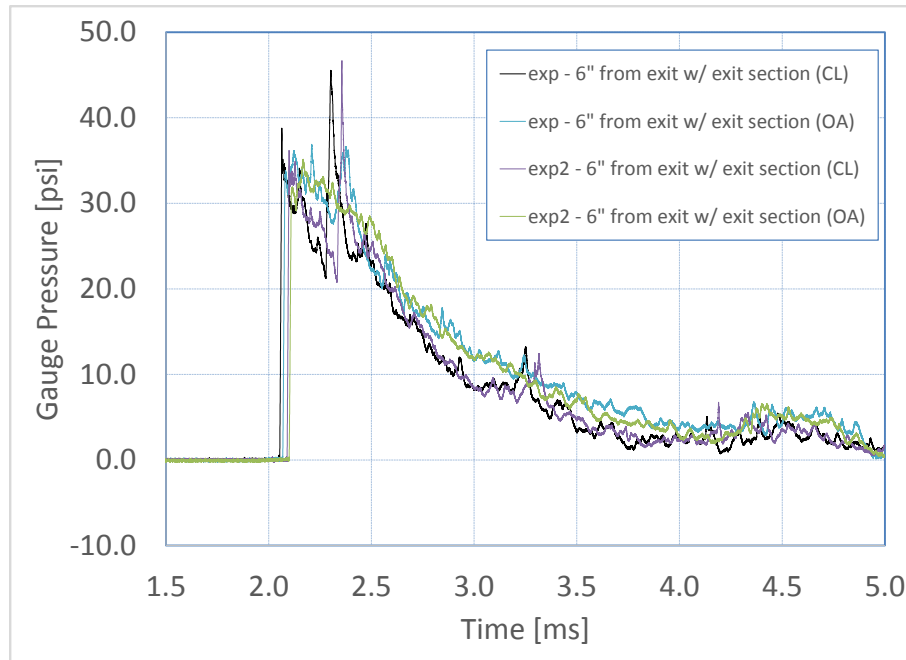


Fig. A-5 Experimental data from pencil gauges inserted 6 inches outside the conical shock tube's exit (i.e., 2.31 m from the charge surface), when a cylindrical exit section is used. Data are shown from 2 experiments, both on and 102 mm off-axis.

List of Symbols, Abbreviations, and Acronyms

Al	aluminum
ALE	arbitrary Lagrangian-Eulerian
C4	Composition C4
EOS	equation of state
JWL	Jones-Wilkes-Lee
TNT	trinitrotoluene

1	DEFENSE TECHNICAL	RDRL WMM D
(PDF)	INFORMATION CTR	D HASH
	DTIC OCA	G CHANEY
		B HALL
2	DIRECTOR	J GYOLAI
(PDF)	US ARMY RESEARCH LAB	D WEYAND
	RDRL CIO L	
	IMAL HRA MAIL & RECORDS	
	MGMT	
1	GOVT PRINTG OFC	
(PDF)	A MALHOTRA	
33	DIR USARL	
(PDF)	RDRL WMP	
	S SCHOENFELD	
	RDRL WMP A	
	S BILYK	
	RDRL WMP B	
	C HOPPEL	
	A DILEONARDI	
	T WEERASOORIYA	
	RDRL WMP C	
	T BJERKE	
	R BECKER	
	RDRL WMP D	
	J RUNYEON	
	R DONEY	
	S SCHRAML	
	RDRL WMP E	
	P SWOBODA	
	RDRL WMP F	
	N GNIAZDOWSKI	
	C CUMMINS	
	RDRL WMP G	
	R EHLERS	
	P DUVALL	
	B HOMAN	
	S KUKUCK	
	R BANTON	
	J BOYD	
	D KOOKER	
	C PECORA	
	B SHOWALTER	
	R SPINK	
	J STARKENBERG	
	RDRL WML C	
	S AUBERT	
	D MEGONNELL	
	B ROOS	
	G SUTHERLAND	

INTENTIONALLY LEFT BLANK.